

# Online simulations of global aerosol distributions in the NASA GEOS-4 model and comparisons to satellite and ground-based aerosol optical depth

Peter Colarco,<sup>1</sup> Arlindo da Silva,<sup>2</sup> Mian Chin,<sup>1</sup> and Thomas Diehl<sup>1,3</sup>

Received 13 July 2009; revised 19 October 2009; accepted 19 January 2010; published 30 July 2010.

[1] We have implemented a module for tropospheric aerosols (GOCART) online in the NASA Goddard Earth Observing System version 4 model and simulated global aerosol distributions for the period 2000–2006. The new online system offers several advantages over the previous offline version, providing a platform for aerosol data assimilation, aerosol-chemistry-climate interaction studies, and short-range chemical weather forecasting and climate prediction. We introduce as well a methodology for sampling model output consistently with satellite aerosol optical thickness (AOT) retrievals to facilitate model-satellite comparison. Our results are similar to the offline GOCART model and to the models participating in the AeroCom intercomparison. The simulated AOT has similar seasonal and regional variability and magnitude to Aerosol Robotic Network (AERONET), Moderate Resolution Imaging Spectroradiometer, and Multiangle Imaging Spectroradiometer observations. The model AOT and Angstrom parameter are consistently low relative to AERONET in biomass-burning-dominated regions, where emissions appear to be underestimated, consistent with the results of the offline GOCART model. In contrast, the model AOT is biased high in sulfate-dominated regions of North America and Europe. Our model-satellite comparison methodology shows that diurnal variability in aerosol loading is unimportant compared to sampling the model where the satellite has cloud-free observations, particularly in sulfate-dominated regions. Simulated sea salt burden and optical thickness are high by a factor of 2–3 relative to other models, and agreement between model and satellite over-ocean AOT is improved by reducing the model sea salt burden by a factor of 2. The best agreement in both AOT magnitude and variability occurs immediately downwind of the Saharan dust plume.

**Citation:** Colarco, P., A. da Silva, M. Chin, and T. Diehl (2010), Online simulations of global aerosol distributions in the NASA GEOS-4 model and comparisons to satellite and ground-based aerosol optical depth, *J. Geophys. Res.*, 115, D14207, doi:10.1029/2009JD012820.

## 1. Introduction

[2] Aerosols scatter and absorb solar and longwave radiation, perturbing the energy balance of Earth's atmosphere [McCormick and Ludwig, 1967; Charlson and Pilat, 1969; Atwater, 1970; Mitchell, 1971]. Aerosols additionally have complex and not yet well-understood effects on cloud brightness [Twomey, 1974] and the occurrence and intensity

of precipitation [Gunn and Phillips, 1957; Liou and Ou, 1989; Albrecht, 1989] and so play a role in modulating Earth's climate and hydrological cycle [e.g., Ramanathan *et al.*, 2001a]. Long-range transport of aerosol pollutants can as well impact the air quality and visibility far from sources [e.g., Prospero, 1999; Jaffe *et al.*, 2003; Bertschi *et al.*, 2004; Colarco *et al.*, 2004]. The extent of anthropogenic influence on the global aerosol system is the determinate and key uncertainty in anthropogenic radiative forcing of Earth's climate system [Intergovernmental Panel on Climate Change, 2007].

[3] Because of this role of aerosols in modulating Earth's climate, a considerable aerosol observing system has evolved, especially since the late 1990s. This observing system includes space-based remote sensing platforms [e.g., Herman *et al.*, 1997; Goloub *et al.*, 1999; King *et al.*, 1999; Kaufman *et al.*, 2002; Stephens *et al.*, 2002; Winker *et al.*, 2003], networks of ground-based sampling [e.g., Malm *et*

<sup>1</sup>Atmospheric Chemistry and Dynamics Branch, Laboratory for Atmospheres, NASA Goddard Space Flight Center, Greenbelt, Maryland, USA.

<sup>2</sup>Global Modeling and Assimilation Office, Laboratory for Atmospheres, NASA Goddard Space Flight Center, Greenbelt, Maryland, USA.

<sup>3</sup>Also at Goddard Earth Science and Technology Center, University of Maryland, Baltimore, Maryland, USA.

*al.*, 1994; Prospero, 1999] and remote sensing instruments [e.g., Holben *et al.*, 1998; Welton *et al.*, 2001], and occasional aircraft campaigns that include detailed in situ sampling and remote sensing measurements [e.g., Ramanathan *et al.*, 2001b; Swap *et al.*, 2003; Reid *et al.*, 2003; Singh *et al.*, 2006]. Despite this progress, however, coordination of these various measurements remains challenging [Diner *et al.*, 2004], and there remain large gaps in both the characterization of aerosol composition (i.e., size, shape, absorption) and the spatial and temporal coverage of these observations (i.e., throughout the vertical column, over bright surfaces, in the vicinities of clouds) [e.g., Chin *et al.*, 2009a].

[4] Chemical transport models (CTMs) have emerged as important tools for filling in these observational gaps, either by formally homogenizing the observing systems through data assimilation [e.g., Collins *et al.*, 2001; Zhang *et al.*, 2008] or by serving as a platform to interpret observations from diverse sources [e.g., Rasch *et al.*, 2001; Chin *et al.*, 2002, 2003; Colarco *et al.*, 2002, 2003; Heald *et al.*, 2006; Matichuk *et al.*, 2007, 2008]. The aerosol models noted above are of a class of “offline” CTMs: the meteorology driving the aerosol simulation is prescribed. By contrast, an “online” simulation couples the dynamics of the aerosol distributions to the atmospheric thermodynamic state so that the solutions are fully interactive and the impact of, for example, variations in aerosol properties can feed back on the system. This online approach has been taken in some air quality forecasting systems [e.g., Jacobson, 1997a, 1997b; Grell *et al.*, 2005] and is the basis for interactive assessment of the impact of aerosol distributions on future climate [e.g., Koch, 2001; Perlitz *et al.*, 2001]. Recently, the European Center for Medium-Range Weather Forecasting (ECMWF) has made strides toward an operational online global aerosol and weather forecasting system that includes prognostic aerosol distributions and a data assimilation capability [Morcrette *et al.*, 2009; Benedetti *et al.*, 2009].

[5] In this paper we introduce a new online aerosol modeling system, based on the merger of a well-known offline aerosol transport model (the Goddard Chemistry, Aerosol, Radiation, and Transport model, GOCART) with the state-of-the-art NASA Goddard Earth Observing System (GEOS) atmospheric general circulation model and data assimilation system. There are a number of advantages of including GOCART online within the GEOS modeling system. The GEOS system routinely performs near-real-time meteorological forecasts; the inclusion of aerosols in this system automatically provides an additional chemical weather forecasting capability. The GEOS system already incorporates data assimilation of meteorological parameters; the inclusion of aerosols will permit an explicit treatment of aerosol effects in the observation operators of current IR sensors (e.g., AIRS, IASI, TOVS), at the same time providing a first step toward a generalized aerosol data assimilation capability. In these respects our effort here is similar to the ECMWF effort noted above. The GEOS system, however, is also being developed with an Earth system modeling capability; the same system used in the forecasting and data assimilation mode can be run as a climate model to explore radiative and chemical feedbacks on the climate system.

[6] This paper seeks to establish the credibility of the baseline aerosol simulations in this new model both in terms of performance relative to other aerosol models and comparisons to observations. We focus here on the quantitative comparison of the simulated aerosol optical thickness to observations from a network of ground-based sun photometers (Aerosol Robotic Network, AERONET) and satellite observations (Moderate Resolution Imaging Spectroradiometer, MODIS, and Multiangle Imaging Spectroradiometer, MISR) over the period 2000–2006. A related study using these simulations [Nowotnick *et al.*, 2009] deals with one aspect of this modeling system in greater detail in a case study of the sensitivity of mineral dust distributions to dust source scheme, augmented by extensive field campaign measurements. The evaluation of the model with respect to other aspects of the global aerosol observing system (e.g., CALIPSO space-based lidar observations) will be the subject of future studies, and we note that the underlying GEOS model core is itself evolving to higher spatial resolutions and newer physical parameterizations.

[7] In section 2 we describe the new modeling system and the data sets used in its evaluation. In section 3 we present the results of our model and the comparisons of simulated aerosol burden, lifetime, and optical thickness to other similar aerosol models and observational data sets. In section 4 we discuss the overall model results. Section 5 provides a brief conclusion.

## 2. Methodology

### 2.1. Model Description

[8] We have implemented an aerosol transport module online within the NASA Global Modeling and Assimilation Office (GMAO) Goddard Earth Observing System version 4 (GEOS-4) atmospheric general circulation model (AGCM) [Bloom *et al.*, 2005]. GEOS-4 is based on the finite-volume dynamical core [Lin, 2004] and contains physical parameterizations based on the National Center for Atmospheric Research (NCAR) Community Climate Model version 3 (CCM3) physics package [Kiehl *et al.*, 1996]. GEOS-4 incorporates version 2 of the Community Land Model (CLM2, Bonan *et al.*, 2002). The Physical-space Statistical Analysis System (PSAS) is the backbone of the meteorological assimilation system in GEOS-4 [Bloom *et al.*, 2005].

[9] GEOS-4 can be run in climate, data assimilation, or replay modes. In climate mode, the initial conditions are set and the model provides a forecast for a specified time. In assimilation mode, the model is run similarly to climate mode, but a meteorological analysis is performed every 6 h to adjust the model temperature, wind, and pressure fields. In replay mode, the model is forced by a previous analysis. By construction, the GEOS-4 replay with an identical version of the model used to generate the analysis reproduces the analysis meteorology exactly. Replay mode allows us to simulate the period of time covered by the previous analysis but without the computational cost of actually running the analysis. This mode is most similar to how offline CTMs work.

[10] The aerosol module incorporated in GEOS-4 is based on the NASA GOCART model as described in Chin *et al.* [2002] and contains components for dust, sea salt, black and organic carbon, and sulfate aerosols. Previously,

GOCART has been run as an offline CTM driven by assimilated meteorology [Chin *et al.*, 2002, 2003, 2007, 2009b]. In GEOS-4, GOCART is run online within the AGCM. Here, by “online” we mean that the aerosol transport and dynamics are consistent with the GEOS-4 AGCM meteorological fields at every time step. This can be contrasted with an offline simulation in which the meteorology at a particular time step is interpolated from the bounding analyses. We note that the aerosols are not radiatively coupled to the AGCM in the version of GEOS-4 used here.

[11] We replay GEOS-4 from the GEOS-DAS CERES analyses [Bloom *et al.*, 2005] for the years 2000–2006. The analyses are available every 6 h at a spatial resolution of  $1.25^\circ$  longitude  $\times 1^\circ$  latitude with 55 vertical layers between the surface and about 80 km. An important caveat in our replay approach is that while we replay the winds, pressures, and temperature fields from the analyses, we do not use their moisture fields, instead allowing the model to develop its own moisture climatology. This approach reduces the GEOS-DAS tendency toward excessive precipitation in the tropics (i.e., the GEOS-DAS system has a dry bias when assimilating moisture observations) and improves the comparison between model and observed precipitation data sets [Bloom *et al.*, 2005]. We note this is a novelty of the online system discussed here, in that offline CTMs generally lack the physical mechanisms to develop their own humidity fields. Additionally, although the model advection and physical processes are conservative of the total air mass, the replayed pressure fields are not; tracer mass concentration is explicitly enforced in our model by requiring the same dry mass of each aerosol tracer before and after the new analysis is introduced in the replay step.

[12] We run the model at the same horizontal resolution as the analyses but reduce the number of vertical levels in the stratosphere so that we run with only 32 vertical levels. The model physical and chemical time step is 30 min; this time step is further split during the finite-volume dynamics [Lin, 2004]. The aerosol fields are initialized from zero and we allow a 3-month spin-up for the period October–December 1999.

[13] Below we summarize our treatment of each aerosol species in our online implementation of GOCART in GEOS-4 in order to document differences from our reference Chin *et al.* [2002] version of GOCART. We note that, as in Chin *et al.* [2002], our aerosols are treated as external mixtures and do not interact with each other. The assumption of external mixing has implications for aerosol optical properties, as internally mixed (e.g., coated) particles may have very different optical properties than their component constituents may imply (e.g., enhanced absorption due to coatings, as in Jacobson [2001]). We acknowledge this limitation in the current model and suggest exploring this further in the future as more detailed aerosol microphysics will be incorporated in the model and permit internal mixing to be considered (e.g., including microphysical mechanisms as in Bauer *et al.* [2008]).

### 2.1.1. Dust

[14] As in Chin *et al.* [2002], the spatial distribution and magnitude of dust sources in our model follows from Ginoux *et al.* [2001] and is based on the association of observed dust source locations with large-scale topographic depressions. We have modified this source map over China

to reflect the influence of recent land use change on dust emissions [Chin *et al.*, 2003]. We additionally incorporate the particle size-dependent threshold wind speed formulation to initiate dust emissions from Marticorena and Bergametti [1995] (their equation (6)). Owing to differences in the GEOS-4 climatology of surface winds relative to previous versions of the GEOS-DAS assimilated meteorology (such as those used in previous GOCART simulations) we have adjusted the global scaling constant for dust emissions (see Ginoux *et al.* [2001] equation (2)) to  $C = 0.375 \mu\text{g s}^2 \text{m}^{-5}$  (Ginoux *et al.* [2001] used  $C = 1 \mu\text{g s}^2 \text{m}^{-5}$  and obtained emissions of  $1814 \text{Tg yr}^{-1}$  for  $0.1\text{--}6 \mu\text{m}$  radius particles; we obtain an average emissions of  $1475 \text{Tg yr}^{-1}$  over that size range). We discretize the dust particle size distribution into eight size bins spaced between  $0.1\text{--}10 \mu\text{m}$  radius, following the size partitioning in Tegen and Lacis [1996]. Four of the size bins are in the range  $1\text{--}10 \mu\text{m}$  radius; for each of these bins we assume the soil mass fraction  $s_r = 0.25$ . Because the particle fall velocity is negligible for submicron particles we group the first four size bins ( $0.1 \mu\text{m} \leq r \leq 1 \mu\text{m}$ ) into a single transported bin but retain the subbin particle size distribution of Tegen and Lacis [1996] for purposes of optics calculation. For purposes of emission, the grouped first bin has soil mass fraction  $s_r = 0.1$ . Our dust removal is by sedimentation, dry deposition, wet removal, and convective scavenging as in Chin *et al.* [2002].

[15] We compute optical properties for each of our size bins assuming that the subbin particle size distribution is described by the functional form  $d(\text{Mass})/d(\ln r) = \text{constant}$  [after Tegen and Lacis 1996]. Assuming sphericity and a constant particle density across the size bin, this implies a power-law distribution for the subbin particle number size distribution (i.e.,  $d(\text{Number})/dr \sim r^{-4}$ ). As for other aerosol species, we assume Mie scattering [Wiscombe, 1980] and refractive indices from the Global Atmospheric Data Set (GADS [Koepke *et al.*, 1997]), although we modify the refractive indices for dust somewhat across the visible part of the spectrum to more closely match a climatology of refractive indices retrieved from the ground-based AERONET sun/sky photometer observations [Holben *et al.*, 1998; Dubovik *et al.*, 2002] at Capo Verde, off the west African coast and under the summer Sahara dust plume. The implications of this choice of refractive indices is a less absorbing dust aerosol at near-UV and visible wavelengths than the GADS inventory would indicate, consistent with recent studies [e.g., Kaufman *et al.*, 2001; Colarco *et al.*, 2002; Sinyuk *et al.*, 2003]. At 550 nm, the single scatter albedo for our 2000–2006 mean dust particle size distribution is 0.93 over Saharan Africa using the refractive indices in this study ( $n_{\text{ref}} = 1.45 - 0.0022i$ ), compared with 0.87 using the GADS refractive indices ( $n_{\text{ref}} = 1.53 - 0.0055i$ ).

### 2.1.2. Sea Salt

[16] By mass, the dominant source of aerosol globally is sea salt produced by wind action at the ocean surface. We are at present not interested in simulating the optically less important and short-lived giant-sized sea salt aerosol particles (dry radius  $> 10 \mu\text{m}$ ), so we consider here only the indirect production mechanism from bursting bubbles [Monahan *et al.*, 1986], as modified by Gong [2003] to account better for the size distribution of small sea salt particles. Accordingly, we simulate the lifecycle of sea salt

aerosols using five size bins spanning the range  $0.03\text{--}10\ \mu\text{m}$  dry radius, where the emissions are a function of the particle size and surface wind speed (*Gong* [2003] equation (2)). We assume the particles undergo hygroscopic growth according to the equilibrium parameterization of *Gerber* [1985] (see also *Gong* et al. [1997]). Aerosol losses due to sedimentation, dry deposition, wet removal, and convective scavenging are as in *Chin* et al. [2002]. The humidified particle size enters our computations of the particle fall velocity, deposition velocity, and optical parameters.

### 2.1.3. Carbonaceous Aerosol

[17] We track separately black and organic carbon aerosols. In what follows, we represent organic carbon aerosols in our model in terms of particulate organic matter (POM, where  $\text{POM} = 1.4 \times$  organic carbon mass, see *Textor* et al. [2006]). The sources of these aerosol particles arise from anthropogenic and natural sources, including fossil fuel, biofuel, and biomass-burning emission sources, and (in the case of organic carbon) from the oxidation of biogenic emissions from plant matter. Our biomass burning source is from the Global Fire Emission Database version 2 (GFEDv2) [*van der Werf* et al., 2006] and provides monthly varying emissions keyed to satellite fire detections. Owing to the heat generated in the fires we distribute their emissions uniformly throughout the planetary boundary layer height in the grid box fire emissions occur in, although we note that recent evidence suggests a significant fraction of wildfire smoke emissions could be injected above the boundary layer [e.g., *Kahn* et al., 2008], which would have impacts on the long-range transport of the smoke. We have time-invariant sources of fossil fuels and biofuels, and a monthly varying climatology of biogenic emissions, following from *Chin* et al. [2002], except that we have modified biofuel and fossil fuel sources in the United States to a monthly varying climatology as in *Park* et al. [2003]. Aerosol losses are by dry deposition, wet removal, and convective scavenging as in *Chin* et al. [2002]. Following *Cooke* et al. [1999] and *Chin* et al. [2002], we account for the chemical processing (“aging”) of the carbonaceous aerosols as a conversion from a hydrophobic to hydrophilic mode with an *e*-folding timescale of 2.5 d [*Maria* et al., 2004]. The hydrophobic component of the aerosol has equivalent optical properties to the hydrophilic component at 0% relative humidity but is not subject to wet removal or convective scavenging processes. The hydrophilic component is subject to these removal processes. The aerosol optical properties are as in *Chin* et al. [2002].

### 2.1.4. Sulfate Aerosols

[18] The treatment of sulfate aerosol cycle is updated somewhat from *Chin* et al. [2002]. We have primary emissions of dimethylsulfide (DMS), sulfur dioxide ( $\text{SO}_2$ ), and sulfate ( $\text{SO}_4$ ). We use the GFEDv2 inventory discussed above to provide monthly varying emissions of  $\text{SO}_2$  from biomass-burning sources.  $\text{SO}_2$  emissions from explosive volcanic injection are based on data from the Global Volcanism Program [*Siebert* and *Simkin*, 2002] and  $\text{SO}_2$  retrievals from the Total Ozone Mapping Spectrometer [*Carn* et al., 2003] and OMI spacecraft instruments and emissions from continuously outgassing volcanoes are from the AeroCom inventories used in similar modeling studies [*Dentener* et al., 2006]. DMS emissions are based on a monthly varying climatology of oceanic DMS concentrations as described in *Chin* et al. [2002]. Anthropogenic

emissions from biofuel and fossil fuel are formulated similarly as for carbonaceous aerosol, as in *Chin* et al. [2002] and *Park* et al. [2003]. The sulfur chemistry cycle follows from *Chin* et al. [2000]. We use prescribed oxidant fields of hydroxyl radical ( $\text{OH}$ ), nitrate radical ( $\text{NO}_3$ ), and hydrogen peroxide ( $\text{H}_2\text{O}_2$ ) from a monthly varying climatology produced from simulations of tropospheric chemistry in the offline Harvard University GEOS-CHEM model [*Bey* et al., 2001], with stratospheric OH superimposed from simulations in the NASA/GMI model [*Kinnison* et al., 2001]. We track separately DMS,  $\text{SO}_2$ ,  $\text{SO}_4$ , and methanesulfonic acid (MSA), which have losses by dry deposition, wet removal, and convective scavenging as in *Chin* et al. [2002]. The treatment of sulfate aerosol optical properties is as in *Chin* et al. [2002].

## 2.2. Data Sets

[19] In order to establish the credibility and performance of our new GEOS-4 modeling system, we compare our simulated aerosol distributions to other similar aerosol models, including a recent version of the offline GOCART CTM driven by the GEOS-4 meteorological analyses [*Chin* et al., 2009b], as well as to several ground-based and satellite observational data sets. We briefly describe those data sets here.

### 2.2.1. AeroCom Models

[20] We compare the results of our simulations to the models participating in the Aerosol Comparisons between Observations and Models (AeroCom) project (<http://nansen.ipsl.jussieu.fr/AeroCom>). The AeroCom initiative was created in 2003 to provide a consistent platform for comparing aerosol models with each other and with various data sets [*Textor* et al., 2006; *Kinne* et al., 2006; *Schulz* et al., 2006]. A recent analysis of 16 global aerosol models participating in AeroCom focused on aerosol lifecycle [*Textor* et al., 2006] and aerosol optical properties [*Kinne* et al., 2006]. We do not attempt here an exhaustive comparison of our model to all of those individually, but rather we highlight the range and mean of the AeroCom models to establish the reasonableness of our model relative to the community state of the art. Included in the AeroCom suite of models is a version of the offline GOCART CTM as driven by the older GEOS-3 meteorological analyses [e.g., *Chin* et al., 2007].

### 2.2.2. Offline GOCART Run with GEOS-4 Analyses

[21] Because of the heritage of our online GEOS-4 simulations with the offline GOCART CTM, we compare our model results of the recent results of the offline GOCART system as driven by the GEOS-4 meteorological analyses [*Chin* et al. 2009b]. Ideally, the principal difference in the two sets of simulations should be the difference between online and offline simulation streams. This is unfortunately not the case, and we note several differences between the online system that is the subject of this paper and the recent offline GOCART results. First, the offline system described in *Chin* et al. [2009b] was run at a coarser spatial resolution ( $2.5^\circ$  longitude  $\times 2^\circ$  latitude with 30 vertical layers) than our online system. Additionally, the *Chin* et al. [2009b] offline model results were driven with more recent inventories for anthropogenic emissions of carbonaceous aerosols and sulfate precursors [*Streets* et al., 2009]. There were as well some variations in the dust and sea salt emission source functions. *Chin* et al. [2009b] use a dust emission scaling

factor of  $C = 0.8 \mu\text{g s}^2 \text{m}^{-5}$  versus the  $C = 0.375 \mu\text{g s}^2 \text{m}^{-5}$  we use in our results, and they adjust the power law dependence on wind speed in the *Gong* [2003] sea salt flux equation to somewhat reduce sea salt emissions. Finally, we note that the version of GOCART implemented online in GEOS-4 was developed independently and from an earlier version of the GOCART system than the *Chin et al.* [2009b] results, so there is likely some variation in particular process algorithms.

### 2.2.3. AERONET

[22] AERONET measures the spectral aerosol optical thickness (AOT) through a ground-based network of sun/sky scanning photometers [*Holben et al.*, 1998]. AERONET has been operating since the early 1990s in support of NASA Earth Observing Satellite validation. Over its lifetime there have been about 400 sites operated, with about 250 sites active as of late 2008. Spectral AOT to an accuracy of  $\pm 0.015$  is determined from direct sun measurements made every 15 min of the spectral transmission at 340, 380, 440, 500, 670, 870, and 1020 nm [*Holben et al.*, 2001]. From the AOT measurements, the Angstrom parameter can be determined as

$$\alpha = -\frac{\ln(\tau_{\lambda_1}/\tau_{\lambda_2})}{\ln(\lambda_1/\lambda_2)}, \quad (1)$$

where  $\tau_\lambda$  is the AOT at two wavelengths  $\lambda_1$  and  $\lambda_2$ . The Angstrom parameter gives important information about particles size: for particles relatively large compared to the wavelength,  $\alpha$  is small ( $\alpha < 1$ ; e.g., dust), while for small particles the AOT varies more strongly with wavelength and  $\alpha > 1$  is typical. Additionally,  $\alpha$  has a dependency on relative humidity in that as particles swell the Angstrom parameter will generally decrease in magnitude. In our analysis we use the Version 2 (<http://aeronet.gsfc.nasa.gov/>), Level 2 (cloud-screened, quality-assured) AERONET direct sun derived AOT product, specifically the AOT at 500 nm and the 440 nm–870 nm Angstrom parameter. Critical to AERONET operation is a uniform calibration and cloud-screening procedure [*Smirnov et al.*, 2000].

### 2.2.4. MODIS

[23] The space-based MODIS provides near-global, daily retrievals of AOT in cloud-free and glint-free conditions using separate algorithms over ocean [*Tanré et al.*, 1996, 1997] and land [*Levy et al.*, 2007a, 2007b]. There are two MODIS instruments. MODIS on the Terra satellite has been operational since early 2000. MODIS on the Aqua satellite has been operational since mid-2002. MODIS-Terra has a daytime equator crossing time of 10:30 AM local and MODIS-Aqua has a daytime equator crossing time of 1:30 PM local. The land and ocean aerosol retrieval algorithms are lookup table based, where the desired aerosol properties are inverted from a table of precomputed spectral radiances that account for different possible size and composition mixtures of aerosols. Over ocean, the AOT is retrieved from radiance measurements at six wavelengths between 550 and 2130 nm, with the AOT product available in seven channels (470, 550, 660, 870, 1240, 1630, and 2130 nm). Over land, a reduced number of channels are available because of the brightness and inhomogeneity of the land surface relative to the ocean; the land retrieval uses the radiances measured at 470, 660, and 2130 nm to provide

AOT at three channels (470, 550, and 660 nm). The uncertainty in the MODIS aerosol products is characterized such that one standard deviation of the retrievals fall within  $\Delta\tau = \pm 0.03 \pm 0.05\tau$  over the ocean and  $\Delta\tau = \pm 0.05 \pm 0.15\tau$  over land relative to collocated AERONET measurements [*Remer et al.*, 2005]. In our analysis we use the land and ocean AOT retrievals valid at 550 nm from the Collection 5 MODIS algorithm products [*Remer et al.*, 2005, 2008].

### 2.2.5. MISR

[24] MISR is aboard the same Terra spacecraft as MODIS-Terra and has also been making retrievals of aerosol properties since early 2000. MISR contains nine push-broom cameras to observe the same point on Earth from nine different angles (nadir,  $\pm 26.1^\circ$ ,  $\pm 45.6^\circ$ ,  $\pm 60.0^\circ$ , and  $\pm 70.5^\circ$ ) and in four spectral bands (446, 558, 672, and 866 nm). Aerosol retrievals are performed using a lookup table approach as well, with retrievals provided at  $17.6 \times 17.6 \text{ km}^2$  horizontal resolution, where constraint of angular information from the multiangle viewing geometry is used to characterize the aerosols and also permits retrievals over bright surfaces [*Martonchik et al.*, 2004; *Abdou et al.*, 2005; *Kahn et al.*, 2005]. The MISR swath width along the ground is at least 360 km, providing global coverage approximately every 9 d. The uncertainty in the MISR AOT retrieval is characterized such that two thirds of the retrievals fall within the larger of 0.05 or  $0.2\tau$  relative to collocated AERONET measurements [*Kahn et al.*, 2005]. The MISR product does not provide a quality assurance (QA) flag as was done for MODIS, but the MISR “best estimate” AOT selected for this study implies high confidence in the aerosol retrieval. We use the latest version of the MISR aerosol retrieval algorithm (version F12\_0022).

## 3. Results

[25] We run the GEOS-4 model with online GOCART aerosols for the period October 1999–December 2006, with the first three months representing a spin-up period. The model is run in a replay mode driven by the GEOS-DAS CERES analyses as described above. We retain the results for the period 2000–2006 for our analysis. We archive the instantaneous snapshot of the model aerosol distributions every 6 h (at 0, 6, 12, and 18 UTC). Time-averaged diagnostic fields relevant to the aerosol budget and lifetime are also archived every 6 h.

### 3.1. Aerosol Budgets and Lifetimes

[26] In this section we discuss the aerosol lifecycle in our GEOS-4 implementation of GOCART relative to similar aerosol models. Table 1 provides a summary of our multiyear average aerosol emissions, burdens, lifetimes, and loss rates. We discuss the GEOS-4 emissions, burdens, and aerosol sink processes and put them in the context of the AeroCom model suite and specifically compare our GEOS-4 results to the offline GOCART model results from *Chin et al.* [2009] (Table 1).

#### 3.1.1. Emissions

[27] Figures 1 and 2 summarize the emissions graphically for our experiment. Figure 1 shows the spatial distribution of the aerosol sources averaged over the period 2000–2006. The major dust sources in the Sahara, the Arabian peninsula, and Asia (the Takla Makan and Gobi deserts) are apparent,

**Table 1.** Global Annual Total Aerosol Emissions and Annual Average Aerosol Burdens, Lifetimes, and Loss Frequencies<sup>a</sup>

Species	Emissions (Tg yr <sup>-1</sup> )	Burden (Tg)	Lifetime (days)	k <sub>wet</sub> (days <sup>-1</sup> )	k <sub>dry</sub> (days <sup>-1</sup> )
Dust	<b>1970</b>	<b>31.6</b>	<b>5.85</b>	<b>0.055</b>	<b>0.116</b>
	3242	38.4	4.33	0.056	0.176
	1789	19.2	4.22	0.084	0.245
	(541–4036)	(1.4–33.9)	(0.92–18.4)	(0.027–0.169)	(0.072–0.995)
Sea salt	<b>9729</b>	<b>23.4</b>	<b>0.88</b>	<b>0.45</b>	<b>0.69</b>
	5056	10.7	0.77	0.40	0.90
	16407	8.3	0.48	0.73	1.60
Black carbon	(2190–117949)	(3.4–18.2)	(0.03–1.59)	(0.11–2.45)	(0.06–2.94)
	<b>10.06</b>	<b>0.243</b>	<b>8.82</b>	<b>0.078</b>	<b>0.036</b>
	10.11	0.239	8.62	0.079	0.037
	11.96	0.229	6.91	0.128	0.028
POM	(7.83–19.34)	(0.113–0.527)	(5.15–15.3)	(0.055–0.175)	(0.005–0.046)
	<b>68.76</b>	<b>1.30</b>	<b>6.90</b>	<b>0.104</b>	<b>0.041</b>
	86.21	1.55	6.56	0.109	0.044
	95.87	1.58	6.07	0.137	0.033
Sulfate (sulfur amount only)	(59.33–137.7)	(0.84–2.14)	(4.12–8.08)	(0.107–2.445)	(0.006–0.094)
	<b>58.73</b>	<b>0.710</b>	<b>4.42</b>	<b>0.194</b>	<b>0.033</b>
	46.12	0.861	5.78	0.146	0.028
	58.18	0.653	4.14	0.224	0.030
	(40.88–77.42)	(0.0369–0.923)	(2.56–6.36)	(0.115–0.340)	(0.003–0.074)

<sup>a</sup>Note. For each cell, the top (bold) number is the result of our GEOS-4 simulations, the second (italicized) number is the result of the offline GOCART model [Chin et al., 2009b], the third number is the average of the AeroCom models (see text), and the final numbers (in parentheses) are the range of the AeroCom models.

as are the lesser dust sources in southern Africa, Patagonia, Australia, and the North American Southwest. Sea salt emissions are at a maximum in the extratropics (the “Roaring Forties” in the Southern Hemisphere, particularly).

Sulfate aerosol emissions and production are highest in the industrial regions of the eastern U.S., central Europe, and Southeast Asia. Carbonaceous aerosols have important anthropogenic sources in the same regions, as well as major

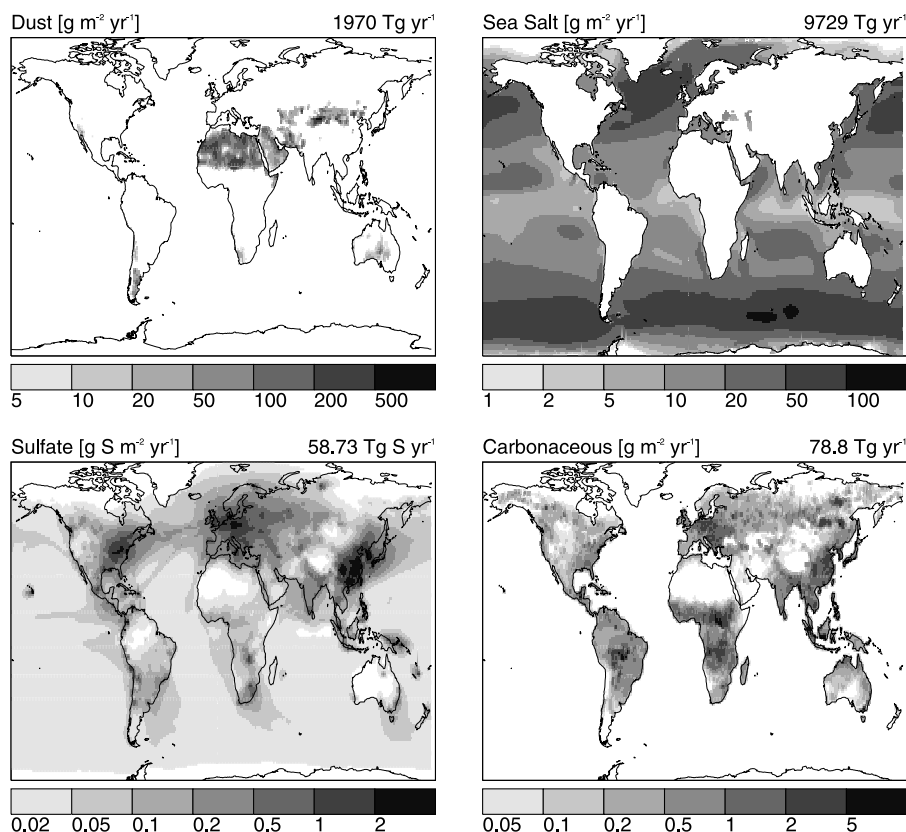


**Figure 1.** Annual average aerosol emissions over the period 2000–2006 used in our model. Results shown are for dust, sea salt (dry mass), sulfate (sulfur mass of direct emissions and chemical production from oxidation of SO<sub>2</sub>), and carbonaceous (BC+POM) aerosol.

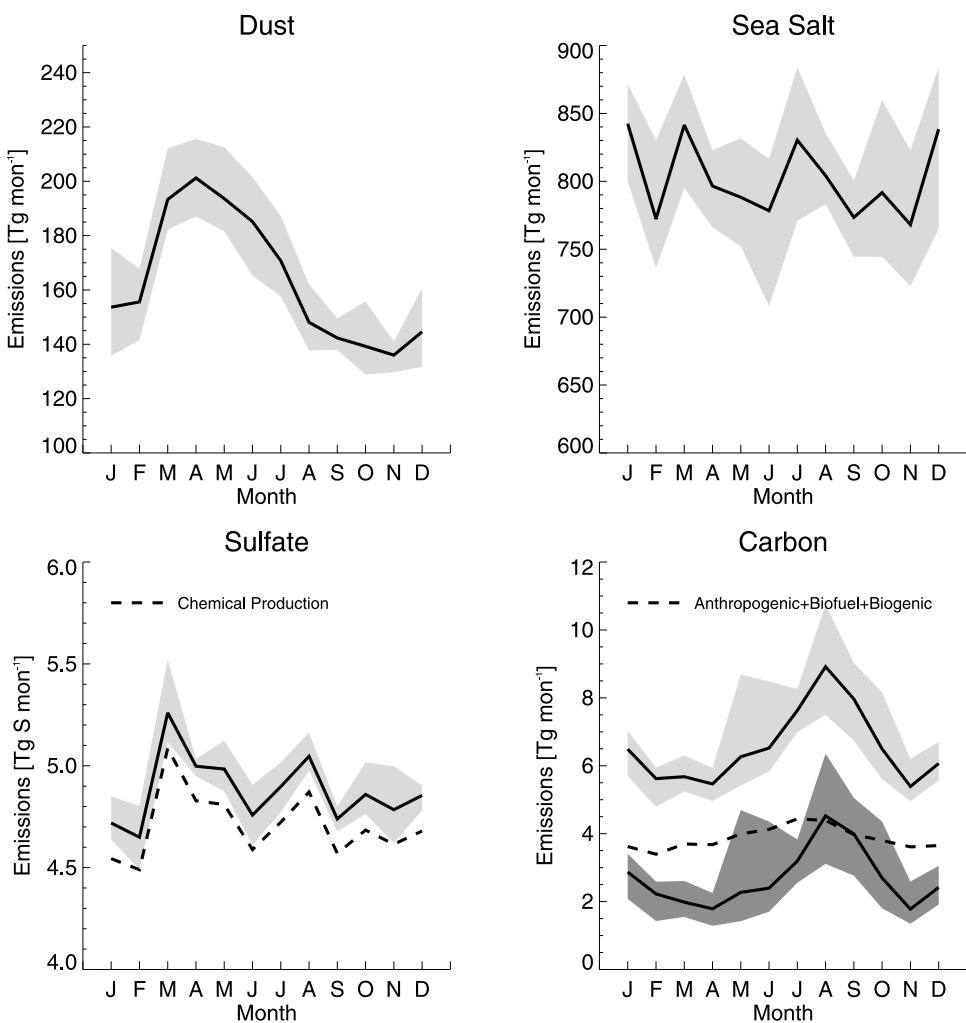


**Figure 2.** Monthly and interannual variability of aerosol emissions in the GEOS-4 model by species. The light shaded region shows the range between the minimum and maximum monthly, globally averaged emissions for the period 2000–2006 and the black line within the shading shows the mean of the emissions over the period 2000–2006. For sulfate aerosols, note that the magnitude is presented in terms of Tg of sulfur per month; the dashed line shows the 2000–2006 average of chemical production of sulfur that goes into the sulfate aerosol. For carbonaceous aerosols, we present the sum of black carbon and particulate organic matter. The darker shaded region in the carbonaceous aerosol plot shows the contribution of biomass burning to emissions and the dashed line shows the sum of anthropogenic, biofuel, and biogenic emissions averaged over the period 2000–2006.

sources from biomass burning in equatorial and southern Africa, South America, and the boreal forests in Siberia and Canada.

[28] Figure 2 shows the climatological monthly aerosol emissions for the period 2000–2006. The shading indicates the maximum and minimum monthly emissions over this period, and so illustrates the range of interannual variability in our model. Also shown are the mean monthly global emissions over this time period (black line). For species other than carbonaceous aerosols the monthly emissions are within 10% of the mean over the period simulated. For dust and sea salt, the emissions are driven by variability in model dynamics (specifically, the surface wind speed) and, in the case of dust, variability in the soil moisture. For sulfate, there is a weak link to the model dynamics via the wind speed dependence of DMS emissions. The dominant source

of sulfate aerosol production is via chemical oxidation of  $\text{SO}_2$ , which incorporates the DMS source and is more strongly linked to the model dynamics by the aqueous phase production of sulfate occurring as  $\text{SO}_2$  is oxidized in cloud and rain water (the mean monthly chemical production of sulfate is shown by the dashed black line, which dominates the overall source of sulfate aerosol and accounts for most of the variability shown in the total source).

[29] The largest interannual variability in aerosol sources is for carbonaceous aerosols (Figure 2). Black carbon emissions account for only about 15% of the mass of total carbonaceous aerosol emissions. About 50–60% of the total carbonaceous emissions are due to anthropogenic, biofuel, and biogenic sources (the dashed black line); we do not account for any interannual variability in these sources. The remaining, but highly variable, contribution to emissions is

due to biomass burning. The interannual variability in biomass burning emissions of carbonaceous aerosols is shown by the darker shaded trace, which varies by as much as 100% about the mean (black line through the shading).

[30] As noted above, in addition to the GEOS-4 results shown in Table 1 we also show the results of the AeroCom model suite and the offline GOCART results. It was not possible to abstract the range of AeroCom model values from the reference paper, so we instead went to the AeroCom website and viewed the data directly. Results from 17 models are used. Not all fields were reported for all models on the website, so when we show the mean and range of values from AeroCom in Table 1 it should be understood that we are showing the mean and range for each species only for the models reporting the relevant quantities on the AeroCom website. Despite this difference, there are only small differences in the mean values of quantities we show in Table 1 relative to the *Textor et al.* [2006] paper (see their Figure 1 and Table 10).

[31] For all species, the annual average emissions in GEOS-4 are within the range of the AeroCom models. We note that this is also true of the offline GOCART results. The greatest diversity in the AeroCom emissions are for dust and sea salt, which is primarily related to what part of the particle size distribution the individual models are simulating but is also related to differences in the meteorology used in the different models. The GEOS-4 emissions differ somewhat from the offline GOCART emissions. The larger dust emission scaling constant used in *Chin et al.* [2009b] results in about 65% greater dust emissions in the offline model, which is not the factor of 2.13 the scaling constant choices in the two models would imply. Although both models use the same winds, the offline model has spatially averaged them to its coarser resolution, so because of the nonlinear relationship of dust emissions to wind speed the offline model would have lower emissions if the scaling constants were identical. The modification to the sea salt emission flux equation results in lower overall sea salt emissions in the offline GOCART, although again the coarser spatial resolution filters out some of the higher surface wind speeds in the meteorological analyses. Emissions are more similar for carbonaceous aerosols, as well as for emissions and production of sulfate, with nearly identical black carbon emissions, somewhat more emissions of POM, and somewhat less production of sulfate in the offline GOCART. As noted above, there were differences in the emission inventories for anthropogenic emissions in these species, but the principle difference appears to be the emission factor choices for determining biomass-burning emissions. In GEOS-4 we use the biome-dependent emission factors from *Andreae and Merlet* [2001] (e.g., 4.76, 0.48, and 0.35 g kg<sup>-1</sup> of dry matter burned, respectively, for POM, black carbon, and SO<sub>2</sub> in savannah and grassland), whereas in the offline GOCART the emission factors chosen have larger magnitudes (11.2, 1, and 1.1 g kg<sup>-1</sup> dry matter in all biomes [*Chin et al.*, 2009b]), corresponding to significantly higher biomass-burning aerosol emissions in GOCART (56 Tg POM yr<sup>-1</sup> versus 30 Tg yr<sup>-1</sup> in GEOS-4). GEOS-4 has a somewhat greater sulfate aerosol source than GOCART. We include in our budget of sulfate sources the chemical production of sulfate aerosol from oxidation of SO<sub>2</sub>. Primary emissions of sulfate are similar in GEOS-4 and GOCART,

so the discrepancy in the total sulfate source is due to chemistry. We point out that different oxidant fields are used in GEOS-4 than in GOCART, and as well that the aqueous production of sulfate from SO<sub>2</sub> reaction with H<sub>2</sub>O<sub>2</sub> will depend on the model hydrological cycle, which is also different in GEOS-4 than in GOCART owing to differences in the meteorology.

### 3.1.2. Burdens

[32] For all species except sea salt, the annual average aerosol burden in GEOS-4 is within the range of the AeroCom models (Table 1). As with emissions, the greatest diversity in the AeroCom models is for dust and sea salt, again reflecting differences in the particle size distributions the various models consider. The burdens of black carbon and sulfate are very similar in the online GEOS-4 and the offline GOCART. As suggested by the emissions, the burden of dust in the offline GOCART is higher than in GEOS-4 but only by about 20% (interestingly, the offline GOCART dust burden is high and outside the range of the AeroCom models). Also as suggested by emissions, the POM burden is about 20% higher in the offline GOCART than in GEOS-4. For sea salt, the burden in GEOS-4 is more than twice the GOCART burden and about three times the magnitude of the average AeroCom burden. We discuss the implications of the high sea salt burden on simulated aerosol optical thickness in sections 3.2 and 4.

### 3.1.3. Lifetimes and Sink Processes

[33] Despite significantly lower emissions of dust in GEOS-4 than in GOCART, the two models develop similar burdens. The explanation is that in GEOS-4 the dust aerosol atmospheric residence time (or lifetime) is about one and a half days longer than in GOCART (5.85 days vs. 4.33 days). Here, the lifetime  $\tau$  is computed as the aerosol burden divided by the loss rate *sink*. In order to separate the aerosol losses into the losses from dry and wet processes, respectively, we compute the loss frequency  $k$  as in *Textor et al.* [2006, equation (7)], computed analogously to the chemical first order loss rate coefficient:

$$k_{\text{wet}} = \frac{1}{\tau} \frac{\text{sink}_{\text{wet}}}{\text{sink}_{\text{wet}} + \text{sink}_{\text{dry}}}; k_{\text{dry}} = \frac{1}{\tau} \frac{\text{sink}_{\text{dry}}}{\text{sink}_{\text{wet}} + \text{sink}_{\text{dry}}} \quad (2)$$

As defined, the greater the removal rate the more efficient that process is at removing aerosols in our model. The aerosol lifetimes and loss frequencies are tabulated in Table 1.

[34] For all species, the aerosol lifetimes in GEOS-4 are within the range of the AeroCom models. This is true also for aerosol loss frequencies, except in the case of POM for the wet loss frequency, which is just outside the lower end of the AeroCom results. In general, however, the aerosol lifetimes in GEOS-4 are somewhat higher than either the mean of the AeroCom results or the GOCART values. The result is that despite lower emissions of dust and carbonaceous aerosols in GEOS-4 relative to GOCART, the burdens are basically similar. The exception is for sulfate, where the GEOS-4 lifetime is shorter than the GOCART lifetime (4.42 d versus 5.73 d), owing to somewhat more efficient removal processes. For carbonaceous aerosols, the removal rates are essentially the same in GEOS-4 as in GOCART.

**Table 2.** Globally, Annually Annual Averaged Aerosol Optical Thickness (AOT [550 nm]) and Mass Extinction Efficiency ( $\beta_{\text{ext}}$ )<sup>a</sup>

Species	AOT	$\beta_{\text{ext}} (\text{m}^2 \text{ g}^{-1})$
Dust	<b>0.034</b> 0.041 0.032  (0.012–0.054)	<b>0.55</b> 0.61 0.99  (0.46–2.05)
Sea salt	<b>0.119</b> 0.021 0.033  (0.020–0.067)	<b>2.59</b> 0.98 3.01  (0.97–7.53)
Black carbon	<b>0.0051</b> 0.0050 0.0041  (0.0017–0.0088)	<b>10.7</b> 10.7 9.41  (5.3–18.9)
POM	<b>0.018</b> 0.018 0.018  (0.006–0.030)	<b>6.94</b> 5.83 5.50  (3.2–9.1)
Sulfate	<b>0.054</b> 0.051 0.035  (0.015–0.051)	<b>12.87</b> 11.59 11.31  (4.2–28.3)

<sup>a</sup>Note. Results are abstracted from Kinne et al. [2006, Table 4]. The separate rows in each table cell are as in Table 1: GEOS-4 (top line, bold), GOCART (second line, italics), AeroCom mean (third line), and AeroCom range (fourth line).

[35] For both dust and sea salt, the removal of aerosol in GEOS-4 is less efficient than in GOCART because of dry removal processes. The total dry removal is the sum of dry deposition due to turbulent mixing in the model surface layer (all species) and removal by gravitational settling (only dust and sea salt). The turbulent dry deposition parameterization is identical for all aerosol species in GEOS-4 and is reasonable for sulfate and carbonaceous aerosols compared to other models, so weaker dry loss process in GEOS-4 for dust and sea salt is attributed to settling. Unfortunately, unraveling that further is beyond the scope of this study. The algorithms used for settling differ somewhat in GEOS-4 relative to GOCART, and there are additional considerations related to the different spatial resolutions used in the two models.

### 3.2. Aerosol Optical Thickness

[36] In this section we focus on evaluating the aerosol distributions simulated by GEOS-4 in terms of the AOT. Relative to aerosol mass, there are considerably more data available to constrain modeled AOT because of the availability of global satellite data sets and the extensive, long running ground-based sun photometer observations from the AERONET [Holben et al., 1998]. We first compare simulated AOT in GEOS-4 to the results of the AeroCom models and offline GOCART, and then we compare to observational data sets.

#### 3.2.1. Comparison of GEOS-4 AOT to Models

[37] In order to derive AOT from modeled mass distributions, a conversion must be applied that implies assumptions about aerosol particle size distribution, composition, and effects of aerosol hygroscopicity on optical properties. This conversion is expressed here in terms of the mass extinction efficiency ( $\beta_{\text{ext}}$ ), which is in practice precomputed in a lookup table for each species as a function of wavelength, relative humidity, and (depending on the species) particle size. In

Table 2 we summarize the various models' globally, annually averaged AOT, as well as the mass extinction efficiency (at  $\lambda = 550$  nm) implied by their AOT and mass burdens (see Kinne et al. [2006], Table 4).

[38] For all aerosol species except sea salt and sulfate, the GEOS-4 mean AOT is within the range of the AeroCom results. The GEOS-4 AOT of carbonaceous and sulfate aerosols is similar to the offline GOCART results, and GEOS-4 has a higher AOT of sea salt and a lower AOT of dust than in GOCART. For dust and POM the GEOS-4 AOT is nearly the same as the mean of the AeroCom results and about 25% higher than the AeroCom mean for black carbon. As already discussed, the GEOS-4 burden of sea salt is considerably higher than in any of the AeroCom models; consequently, the AOT due to sea salt is also high. The sulfate AOT is only slightly outside the range of the AeroCom models. Both the sulfate mass burden and mass extinction efficiency for sulfate in GEOS-4 are about 10% greater than the AeroCom mean values, but it should be stressed that some of the AeroCom models compensate for high or low mass burdens with lower or higher mass extinction efficiencies to produce AOT values somewhere near the mean [Kinne et al., 2006]. It should be noted, for example, that although the offline GOCART burden of sea salt is higher than the AeroCom mean, its AOT is lower and the mass extinction efficiency used is on the low end of the AeroCom models. This is not necessarily significant of anything, as the mass extinction efficiency and burden are both a function of what part of the particle size distribution is considered in the model. Here, though, the significant difference in the GEOS-4 and GOCART mass extinction efficiencies for sea salt are related to the less efficient loss processes in GEOS-4, which favors retaining the more optically efficient part of the size spectrum. We point out, however, that all of the GEOS-4 and GOCART simulated mass extinction efficiencies are within the range of the AeroCom models.

#### 3.2.2. Comparison of GEOS-4 AOT to Observational Data Sets

[39] In the following we compare our model results to observations of the AOT from ground-based and satellite measurements. In the results that follow, we make one correction to the model based on the previous discussion. We have already identified that the sea salt aerosol burden in the model is high and outside the bounds of the AeroCom models despite reasonable emissions (Table 1). The explanation for this is in the much slower sea salt aerosol loss in GEOS-4 relative to other models, particularly in terms of dry removal processes. This plays out in the AOT by leading to much larger sea salt component AOT than in the AeroCom models (Table 2). The improvement of the sea salt component in the model is beyond the scope of this study, so in the remainder of the paper we scale our sea salt burdens by a factor of 0.5 (i.e., we cut the sea salt burden in half) in order to facilitate and improve comparison to observational data sets.

##### 3.2.2.1. Comparisons With AERONET

[40] We compare the simulated aerosol optical thickness and Angstrom parameter from the model with observations from AERONET. Our approach is to construct a consistent database of monthly mean AERONET and model spectral AOT values. We bin the AERONET observations at a

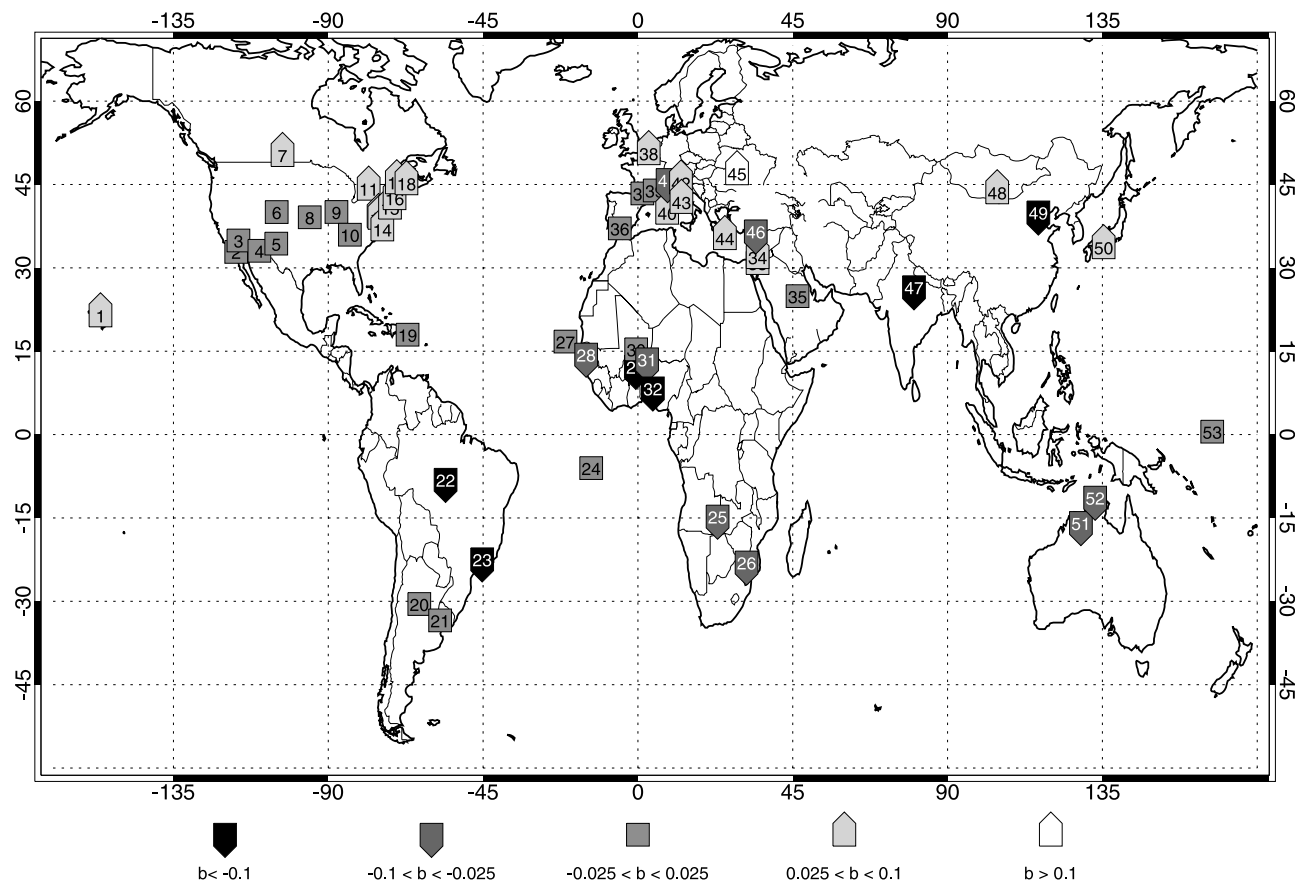


**Figure 3.** Map showing locations of 53 AERONET sites used in this study (see Table 3 for corresponding site names). The symbol indicates the model bias in AOT relative to the observations, with an upward-pointing symbol indicating the model is biased high and downward-pointing symbol indicating the model is biased low. The shading indicates the magnitude of the bias.

6-h time resolution centered at our model synoptic output times of 0, 6, 12, and 18 UTC. The monthly mean of the AERONET AOT is the weighted average of the binned AERONET data in a month, where the mean of each 6-h time bin is weighted by the number of observations that compose it. In order not to bias the results by erroneous or anomalous observations (e.g., clouds that slip through the cloud screening) we require a minimum of four observations per time bin and four valid time bins per month to compose a monthly mean. The model AOT at 500 nm is sampled and weighted consistently with that (i.e., we make the model monthly mean AOT at a site using only times when AERONET had measurements). The monthly mean Angstrom parameter is composed in a similar fashion.

[41] Figure 3 shows the distribution of AERONET sites used in our study. We have selected only sites with three or more valid monthly means for each month (each of January, February, etc.) during the period 2000–2006. This selection process reduces us from several hundred potential AERONET sites to only 53 sites, but these sites have long-term, high-quality records of the total column aerosol burden over our simulation period. Table 3 shows the names of each site, the Principal Investigator (PI), and its location. Additionally, Table 3 and Figure 3 summarize the comparison of our model to the 53 selected AERONET sites. In Figure 3 each AERONET site has an associated shaded symbol where the

symbol's orientation and shading indicate the model's AOT bias relative to the observations. Table 3 gives the number of months for which the sites and model were compared, the correlation coefficient, bias, and skill score. The general pattern is that (1) the model is biased low in AOT in biomass burning influenced regions in South America and Southern Africa, (2) the model AOT is similarly biased low in the dust and biomass burning influenced regions in Sahelian Africa, (3) the model AOT is similar in magnitude to the observed AOT across the western United States (although we point out that the AOT is low in magnitude at these sites), (4) the model AOT is generally biased high in the eastern United States and anthropogenic pollution influenced sites in Europe, and (5) the model AOT is low compared to Asian sites influenced by mixtures of dust and pollution (e.g., Kanpur, India (#47) and Beijing).

[42] Figures 4–7 show the comparison of the model AOT and Angstrom parameter to AERONET observations at four sites representing different aerosol regimes. Similar plots are made for all 53 sites shown in Figure 3; we show only four sites here for brevity and for their representation of different aerosol environments. Each panel shows the time series, a scatter plot, and a relative distribution (PDF) of the model and observed values of AOT and Angstrom parameter, as well as some statistics of the comparison: number of months compared, correlation coefficient ( $r$ ), absolute bias, root-

**Table 3.** Summary of Statistics for GEOS-4/AERONET Comparisons<sup>a</sup>

#	Site and PI	Lat	Lon	h	n	$r_\tau$	$b_\tau$	$s_\tau$	$r_\alpha$	$b_\alpha$	$s_\alpha$
(1)	Coconut Island (PI: Brent Holben)	21.43	-156.21	0	47	0.55	0.04	0.59	0.64	0.09	0.61
(2)	La Jolla (PI: Robert Frouin)	32.87	-116.75	115	54	0.36	-0.01	0.61	0.44	-0.28	0.61
(3)	Rogers Dry Lake (PI: van den Bosch)	34.93	-116.12	680	62	0.74	0.02	0.86	0.68	-0.22	0.80
(4)	Maricopa (PI: Brent Holben)	33.07	-110.03	360	68	0.69	0.01	0.85	0.43	-0.20	0.59
(5)	Sevilleta (PI: Doug Moore)	34.35	-105.12	1477	71	0.65	-0.00	0.65	0.56	-0.26	0.66
(6)	BSRN BAO Boulder (PI: Brent Holben)	40.04	-104.99	1604	63	0.53	-0.01	0.54	0.61	-0.34	0.48
(7)	Bratts Lake (PI: Bruce McArthur)	50.28	-103.30	586	69	0.52	0.03	0.58	0.79	-0.38	0.69
(8)	KONZA EDC (PI: David Meyer)	39.10	-95.39	341	69	0.78	-0.01	0.62	0.52	-0.37	0.70
(9)	BONDVILLE (PI: Brent Holben)	40.05	-87.63	212	80	0.64	0.02	0.65	0.41	-0.16	0.50
(10)	Walker Branch (PI: Brent Holben)	35.96	-83.71	365	55	0.76	0.02	0.84	0.49	-0.41	0.53
(11)	Egbert (PI: Norm O'Neill)	44.23	-78.25	264	50	0.76	0.06	0.88	0.68	-0.40	0.66
(12)	MD Science Center (PI: Brent Holben)	39.28	-75.38	15	83	0.83	0.05	0.80	0.40	-0.39	0.47
(13)	GSFC (PI: Brent Holben)	38.99	-75.16	87	84	0.83	0.05	0.82	0.70	-0.33	0.74
(14)	COVE (PI: Brent Holben)	36.90	-74.29	37	77	0.80	0.06	0.82	0.27	-0.36	0.52
(15)	CCNY (PI: Barry Gross)	40.82	-72.05	100	56	0.85	0.04	0.81	0.68	-0.23	0.66
(16)	Billerica (PI: Steve Jones)	42.53	-70.73	82	42	0.85	0.04	0.81	0.72	-0.27	0.80
(17)	CARTEL (PI: Alain Royer and Norm O'Neill)	45.38	-70.07	300	54	0.70	0.05	0.83	0.65	-0.30	0.61
(18)	Howland (PI: Brent Holben)	45.20	-67.27	100	63	0.72	0.05	0.83	0.52	-0.41	0.53
(19)	La Parguera (PI: Brent Holben)	17.97	-66.96	12	52	0.84	-0.02	0.72	0.85	0.07	0.74
(20)	Cordoba-CETT (PI: Brent Holben)	-30.48	-63.54	730	62	0.19	-0.01	0.44	0.41	-0.13	0.44
(21)	CEILAP-BA (PI: Brent Holben)	-33.43	-57.50	10	77	0.09	-0.02	0.33	0.20	-0.29	0.53
(22)	Alta Floresta (PI: Brent Holben)	-8.13	-55.90	277	65	0.83	-0.16	0.49	0.78	0.14	0.58
(23)	Sao Paulo (PI: Paulo Artaxo)	-22.44	-45.26	865	61	0.43	-0.11	0.35	0.44	0.02	0.67
(24)	Ascension Island (PI: Brent Holben)	-6.02	-13.59	30	51	0.50	-0.00	0.75	0.67	0.14	0.51
(25)	Mongu (PI: Brent Holben)	-14.75	23.15	1107	77	0.26	-0.08	0.37	0.62	-0.10	0.33
(26)	Skukuza (PI: Stuart Piketh and Brent Holben)	-23.01	31.59	150	81	0.49	-0.08	0.33	0.41	-0.10	0.44
(27)	Capo Verde (PI: Didier Tanré)	16.73	-21.07	60	67	0.77	0.00	0.79	0.42	-0.04	0.46
(28)	Dakar (PI: Didier Tanré)	14.39	-15.04	0	55	0.52	-0.04	0.69	0.33	-0.14	0.31
(29)	Ouagadougou (PI: Didier Tanré)	12.20	-0.60	290	67	0.52	-0.12	0.27	0.42	-0.06	0.71
(30)	Agoufou (PI: Philippe Goloub)	15.34	-0.52	305	40	0.35	-0.01	0.58	-0.08	-0.08	0.42
(31)	Banizoumbou (PI: Didier Tanré)	13.54	2.66	250	69	0.58	-0.04	0.55	0.18	-0.10	0.58
(32)	Ilorin (PI: Rachel T. Pinker)	8.32	4.34	350	50	0.56	-0.24	0.14	0.83	-0.05	0.90
(33)	SEDE BOKER (PI: Arnon Karniel)	30.85	34.78	480	75	0.56	0.07	0.77	0.72	-0.13	0.85
(34)	Nes Ziona (PI: Arnon Karniel)	31.92	34.79	40	70	0.47	0.05	0.68	0.76	-0.24	0.88
(35)	Solar Village (PI: Naif Al-Abbad)	24.91	46.40	764	78	0.74	-0.01	0.77	0.68	-0.17	0.33
(36)	El Arenosillo (PI: Cachorro Revilla)	37.10	-5.27	0	60	0.66	0.02	0.83	0.70	-0.25	0.78
(37)	Le Fauga (PI: Mougenot and Dedieu)	43.38	1.28	193	45	0.34	0.01	0.67	0.60	-0.37	0.72
(38)	Lille (PI: Philippe Goloub)	50.61	3.14	60	54	0.57	0.06	0.75	0.66	-0.18	0.82
(39)	Avignon (PI: Frédéric Baret)	43.93	4.88	32	75	0.56	0.01	0.76	0.75	-0.34	0.88
(40)	IMC Oristano (PI: Didier Tanré)	39.91	8.50	10	41	0.44	0.06	0.66	0.73	-0.06	0.72
(41)	Ispra (PI: Giuseppe Zibordi)	45.80	8.63	235	80	0.51	-0.03	0.75	0.50	-0.36	0.74
(42)	Venise (PI: Giuseppe Zibordi)	45.31	12.51	10	74	0.51	0.08	0.71	0.71	-0.26	0.83
(43)	Rome Tor Vergata (PI: Gian Paolo Gobbi)	41.84	12.65	130	61	0.51	0.08	0.68	0.61	-0.21	0.77
(44)	FORTH CRETE (PI: Andrew Clive Banks)	35.33	25.28	20	48	0.22	0.10	0.61	0.69	-0.13	0.76
(45)	Moldova (PI: Brent Holben)	47.00	28.82	205	64	0.54	0.10	0.77	0.62	-0.23	0.75
(46)	IMS-METU-ERDEMLI (PI: Brent Holben)	36.56	34.26	3	53	0.25	-0.05	0.47	0.59	-0.37	0.75
(47)	Kanpur (PI: Holben, Singh, Tripathi)	26.51	80.23	123	64	0.19	-0.31	0.58	0.79	-0.04	0.74
(48)	Dalanzadgad (PI: Brent Holben)	43.58	104.42	1470	75	0.78	0.06	0.84	0.34	-0.54	0.21
(49)	Beijing (PI: Chen and Goloub)	39.98	116.38	92	59	0.74	-0.32	0.41	0.66	-0.34	0.78
(50)	Shirahama (PI: Brent Holben)	33.69	135.36	10	67	0.82	0.05	0.85	0.73	-0.26	0.77
(51)	Lake Argyle (PI: Ross Mitchell)	-15.89	128.75	150	46	0.95	-0.06	0.27	0.64	0.08	0.56
(52)	Jabiru (PI: Ross Mitchell)	-11.34	132.89	30	45	0.83	-0.09	0.19	0.65	0.14	0.51
(53)	Nauru (PI: Rick Wagener)	0.52	166.92	7	53	0.48	-0.02	0.74	0.50	0.45	0.65

<sup>a</sup>Note. Shown are the site location number (Figure 3), name and PI, latitude, longitude, and elevation (h in [m]) for each site, the number of monthly means compared (n), as well as the correlation coefficient (r), bias (b), and skill (s) for both AOT ( $\tau$ ) and Angstrom parameter ( $\alpha$ ).

mean-square variance, skill score, and linear fit parameters. The skill score follows from Taylor [2001, equation (4)] and assesses the performance of the model in terms of both its correlation and variance relative to the observations. As defined, the skill score approaches zero as the correlation becomes negative or the variance approaches either zero or infinity and approaches unity as the model variance approaches the observed variance and the correlation approaches 1.

[43] GSFC (Figure 4, #13 in Figure 3 and Table 3) is dominated by anthropogenic aerosols. The model captures the pronounced seasonal variability in the observed AOT

and is well correlated with both the AOT ( $r = 0.83$ ) and Angstrom parameter ( $r = 0.70$ ) at this site, but with a high bias in the AOT ( $b = 0.054$ ) and low bias in the Angstrom parameter ( $b = -0.326$ ).

[44] Alta Floresta (Figure 5, #22) is influenced by seasonally varying biomass burning. Again, the model is well correlated and has similar seasonal variability to the observed AOT ( $r = 0.83$ ) and Angstrom exponent ( $r = 0.78$ ), importantly capturing the annual peak in AOT due to biomass burning. Here, however, the model is biased low relative to the observed AOT ( $b = -0.158$ ) and biased slightly high relative to the Angstrom parameter ( $b = 0.135$ ). The

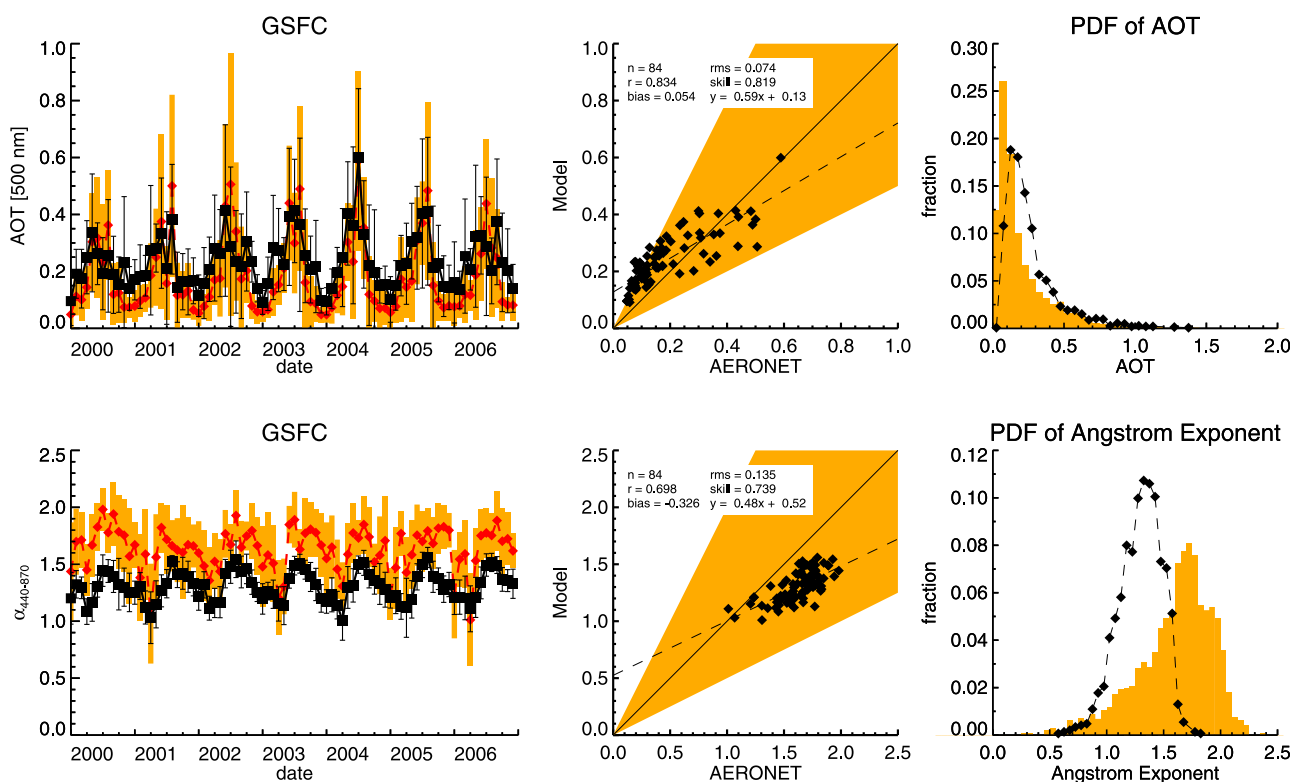


**Figure 4.** Model versus AERONET AOT and Angstrom parameter comparisons at GSFC. In each panel we show a time series, scatterplot, and fractional distribution histogram of the model and AERONET observations. In the time series, the model monthly means and standard deviation about the mean are shown in the black line and symbols. The AERONET monthly means are indicated with the red line and symbols, with the standard deviation about the monthly mean indicated by the orange bars. In the scatter plot, the range of the 1-2 and 2-1 lines are indicated in the orange shading. In the PDF plot, the model is indicated by the black symbols and line, and the AERONET observations are indicated by the orange bars.

underestimate in the AOT is most evident during the peak AOT of the biomass burning season (August–September), and varies from year to year, where the difference between the model and observations is most pronounced in 2002 and 2006, whereas in 2004 and 2005 the model almost captures the observed peak in AOT.

[45] Capo Verde (Figure 6, #27) is influenced by transport of dust from Saharan sources. The model is well correlated with the AOT ( $r = 0.77$ ) and captures the seasonal variability in the dust loading with a slight high bias ( $b = 0.002$ ) but is less well correlated with the Angstrom parameter ( $r = 0.42$ ) and is biased low ( $b = -0.039$ ). Note that in contrast to GSFC and Alta Floresta, the Angstrom exponent is negatively correlated with the AOT, which is consistent with the assertion that the site is dominated by dust aerosols: as the dust load increases, the importance of large particles to AOT increases and the Angstrom parameter decreases. The model tends to underestimate the observed Angstrom parameter at times when the model overestimates the AOT, suggesting that the simulated dust loading is too high at certain parts of the year (e.g., latter half of 2000).

[46] Beijing (Figure 7, #49) is influenced both by dust from the Takla Makan and Gobi deserts as well as anthropogenic pollutants. The model is again well correlated in the AOT ( $r = 0.74$ ) but has a significant low bias ( $b = -0.32$ ).

The correlation with the Angstrom parameter is somewhat more modest ( $r = 0.66$ ) and the bias is also low ( $b = -0.34$ ). The seasonal peak in the simulated Angstrom parameter is correlated with the peak in the model AOT, and at those peaks the modeled Angstrom parameter is similar in magnitude to the observed values. Although the model peak AOT is significantly less than the observed peak in the AOT, the similarity between the modeled and observed Angstrom parameter at these times suggests a similar composition of the modeled aerosol load to what is observed. At times of year when the observed and simulated AOT are at a minimum, however, the model significantly underestimates the Angstrom parameter, which suggests that the aerosol composition in the model is relatively dominated by dust as opposed to pollution, which would be more consistent with the observations. We point out that our aerosol emissions data set for anthropogenic pollutants is based on 1995 numbers and so is likely inadequate for how aerosol loads have changed in China in recent years.

[47] Figure 8 shows a comparison of all the monthly means we have evaluated from the 53 selected AERONET sites over the period 2000–2006, presented as a scatter plot of the model AOT versus the observed AOT, and likewise for the Angstrom parameter. Overall, the model is well correlated with the observed AOT but underestimates its

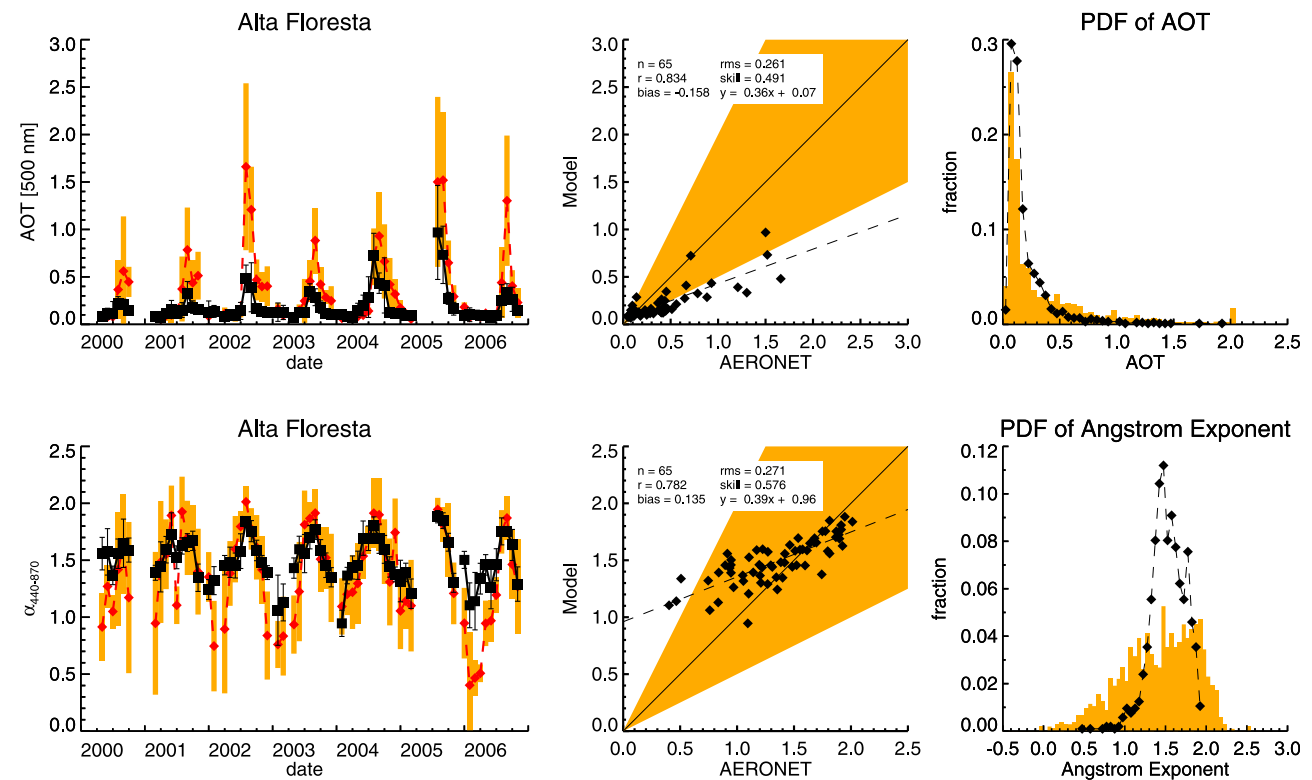


Figure 5. As in Figure 4 but for Alta Floresta.

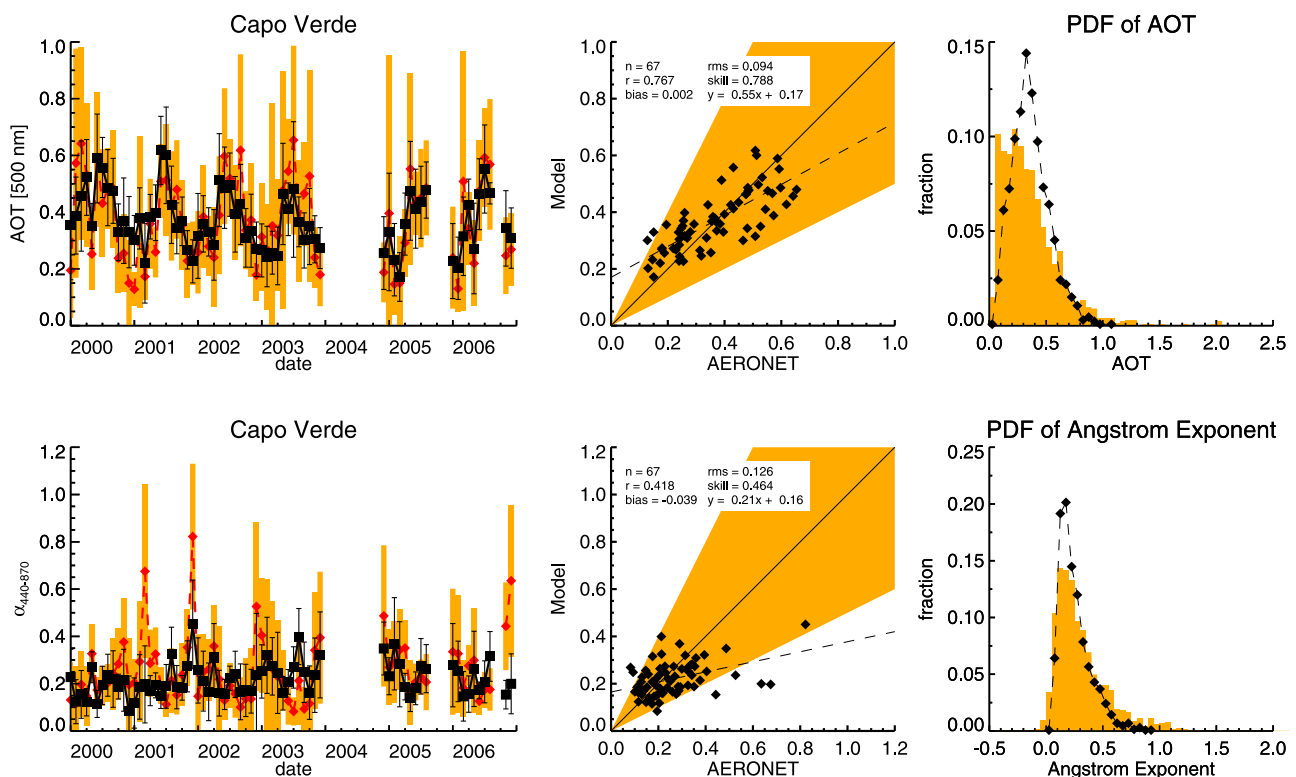
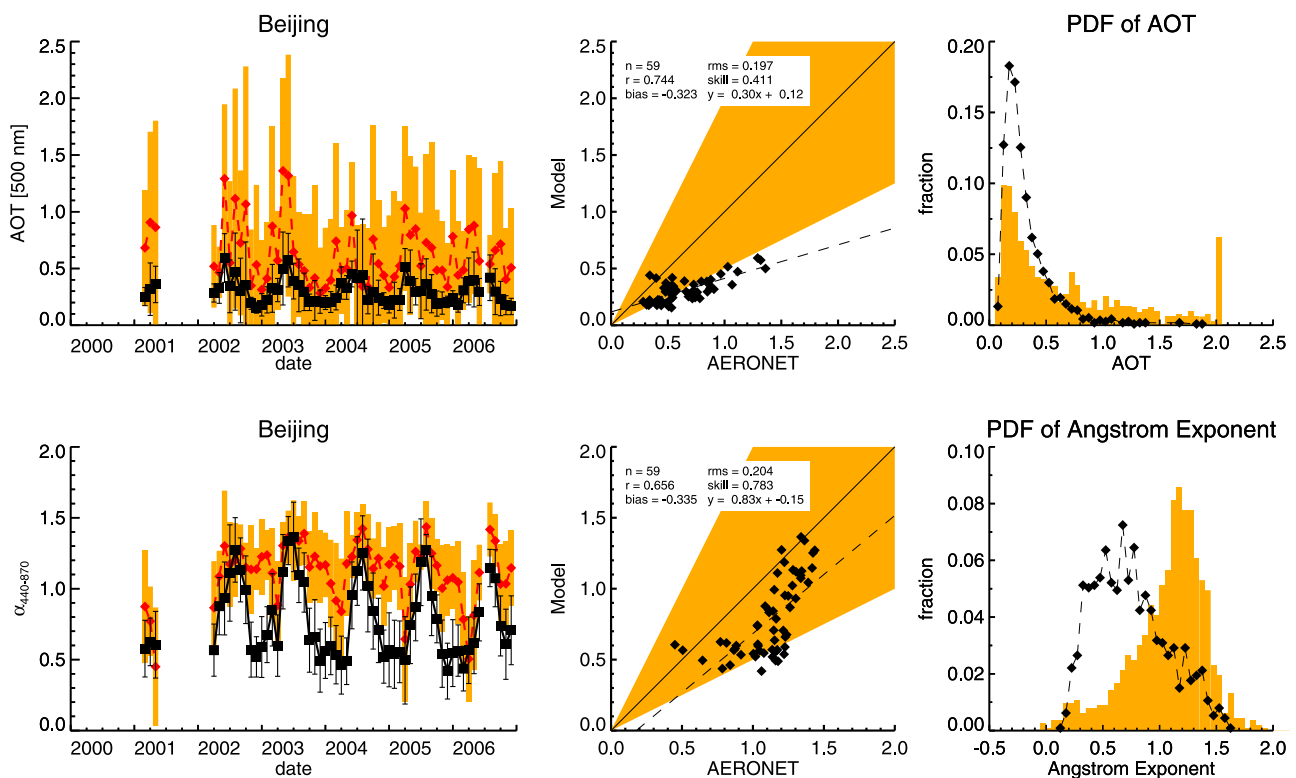


Figure 6. As in Figure 4 but for Capo Verde.



**Figure 7.** As in Figure 4 but for Beijing.

magnitude, as indicated by the slope of the linear model fitting the scatter plot ( $m = 0.48$ ,  $r = 0.707$ ). The model is actually better correlated with the Angstrom parameter observations ( $r = 0.810$ ), but likewise is less than the observed magnitude ( $m = 0.63$ ) with a low bias ( $b = -0.196$ ).

### 3.2.2.2. Comparisons to MODIS

[48] For purposes of comparing the model to the MODIS observations we have begun with the Level 2 MODIS AOT retrievals, available nominally at a  $10 \times 10 \text{ km}^2$  spatial resolution. We construct a gridded satellite product consistent with the formal construction of the MODIS Level 3

gridded products. That is, we aggregate the individual retrievals to the model's  $1.25^\circ \times 1^\circ$  spatial resolution. In the aggregation step, the grid-box mean AOT is determined by weighting the individual retrievals by their quality assurance (QA) flags. QA flags indicate the level of reliability of the retrievals, with values ranging from 0 (lowest quality) to 3 (highest quality). This aggregation and weighting is performed with MODIS data available  $\pm 3$  h of the model synoptic output times (0, 6, 12, and 18Z). The monthly mean AOT of the satellite observations is formed from this aggregated data set by weighting the grid-box average AOT

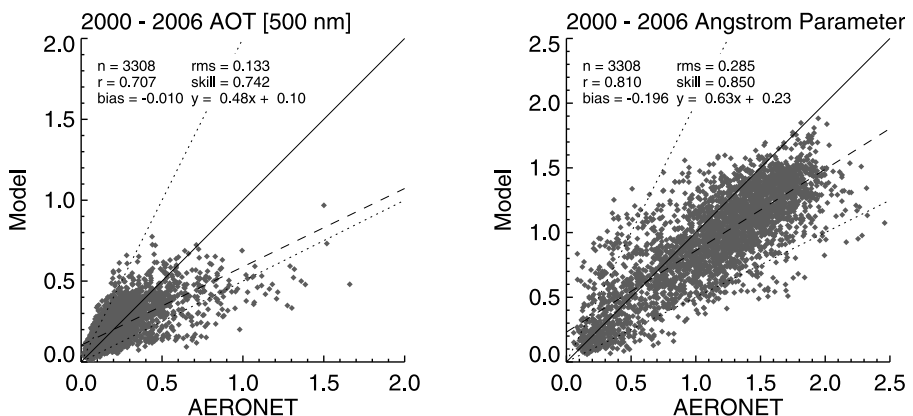


**Figure 8.** Scatterplot of model versus AERONET AOT (left) and Angstrom parameter (right) at all 53 sites for all valid monthly means during the period 2000–2006. We indicate the 1-1 line with the solid line, and 1-2 and 2-1 lines with the short dashed lines, and the line of best fit with the long dashed line.

for each synoptic time by its grid-box total QA value. The monthly mean of the model AOT is formed by sampling the model AOT at each synoptic time at points where the MODIS retrievals exist and weighting each model grid-box AOT with the same MODIS grid-box QA weighting. The result is a monthly mean of the model AOT with the model sampled only at times and locations where MODIS makes observations.

[49] The approach described above of weighting and sampling the model AOT values in a fashion consistent with the satellite observations is obviously of importance when considering, e.g., data assimilation of satellite AOT measurements. It is not, however, an approach we have seen commonly applied to many modeling studies. *Chin et al.* [2004] and *Mitchuk et al.* [2007, 2008] describe similar approaches to sampling and comparing model output to satellite observations, but do not show what effect this strategy has on the comparison. More typically, when the model monthly mean AOT is compared to satellite observations it is shown as the average of the model fields at all synoptic output times (i.e., as was done above in our budget analysis).

[50] In the spirit of putting the sampling approach described above on a better foundation we consider here several alternative approaches to constructing the model monthly mean for comparison with satellite observations. The “sampled” approach is the method described above. In the “unsampled” approach we take the simple mean of the model AOT output at all synoptic times with no weighting for satellite observations. The “swath” approach is somewhere in the space between the sampled and unsampled approaches; in the swath approach we mask out the model AOT in locations outside of the MODIS Terra observational swath before composing the monthly mean. This approach amounts to selecting the model aerosol fields at times consistent with the MODIS observations and includes all points where MODIS potentially could have made a retrieval (i.e., we do not exclude cloud cover, bright surfaces, or sun glint in this approach). As we will discuss shortly, the swath approach has results essentially identical to the unsampled approach, so we will not illustrate or tabulate its results.

[51] Figures 9 and 10 show the 7-year average of the MODIS Terra 550 nm AOT and the GEOS-4 model AOT for the period 2000–2006. Figure 9 shows the unsampled monthly mean of the model AOT compared to the satellite observations, while Figure 10 shows the sampled model comparison. On the left half of each figure we show the satellite average AOT (top) and the model average AOT (bottom). On the right half of each figure we show a difference plot of the long-term average of the model and satellite AOT (top) and a plot of the correlation of the model and satellite monthly means at each grid box.

[52] Similarities between the satellite and model apparent in both comparisons include the magnitude and position of the dust plume coming out of Africa, the relatively high aerosol loading along the Indian base of the Tibetan plateau and in the region of the Takla Makan desert and eastern China, and the Asian pollution plume crossing the northern Pacific Ocean. There are notable differences as well: the model underestimates the aerosol loading in the western United States and in the biomass-burning-dominated regions in South America and southern Africa, the model

overestimates the aerosol loading in the northern Atlantic and northern Pacific, and the model overestimates the aerosol loading in the southern ocean. Generally speaking, the model is well correlated with the satellite monthly means (60% of grid points have  $r > 0.4$ ) over both ocean and land, with notably poorer correlation in the southern ocean, northern Atlantic Ocean, and the ocean west of Central America (where the model had enhanced AOT relative to the observations).

[53] Although the features in both model sets are similar, there are notable differences. First, the unsampled model AOT (Figure 9) is visibly “smoother” in appearance than in the sampled case (Figure 10). Second, the global mean AOT is greater in the unsampled case than in the sampled case. This is notably apparent in several ocean regions, including the sea salt band in the “Roaring Forties” and the anthropogenic export plumes between North America and Europe and between Asia and North America. The difference plots in Figures 9 and 10 reveal these features, as well as making clear also that the unsampled long-term average AOT is greater in primarily anthropogenic polluted regions in North America (U.S. east coast), central Europe, and Southeast Asia. The sampled model results would suggest essentially no bias in the long-term average AOT between the model and MODIS AOT on the U.S. east coast, a small high bias in the model over central Europe, and a significant low bias over Southeast Asia. The unsampled model, however, shows a high bias in the model in all three regions. On the other hand, there are minimal differences between these two approaches in the western United States, the Saharan dust plume from North Africa, or in biomass burning influenced regions in South America and Southern Africa. The correlations of the model observations are also affected, mainly in the enhanced positive correlation under the Saharan dust plume and somewhat less negative correlation west of Central America in the sampled model case, as well as the more apparent negative correlation near Antarctica in the unsampled model case. We will discuss the differences of the sampled and unsampled model monthly mean AOT further in the Discussion (section 4) and restrict ourselves to considering the sampled monthly mean for remainder of this section.

[54] We considered the comparison of the model to satellite AOT in 20 regions over land and ocean illustrated in Figure 11. Figure 12 shows the temporal variability of the satellite and model monthly mean AOT for several of those regions. Over the land, globally the MODIS AOT  $\tau_{550} = 0.21$  and the sampled model AOT  $\tau_{550} = 0.17$  is well correlated with the MODIS observations ( $r = 0.75$ ). For brevity, we graphically show the same analysis for South America, the western United States, and Southeast Asia. The statistics in these and other land regions from Figure 11 are shown in Table 4. The analysis for South America is similar to what was shown with the AERONET data: the model significantly underestimates the AOT in this region, particularly in the peak biomass burning season (August–September). In the western United States the model AOT is about half of the MODIS AOT magnitude but is well correlated ( $r = 0.73$ ). In Southeast Asia the model AOT also underestimates the MODIS AOT magnitude, notably in 2003 when there was greatly enhanced biomass burning from wildfires in Siberia.

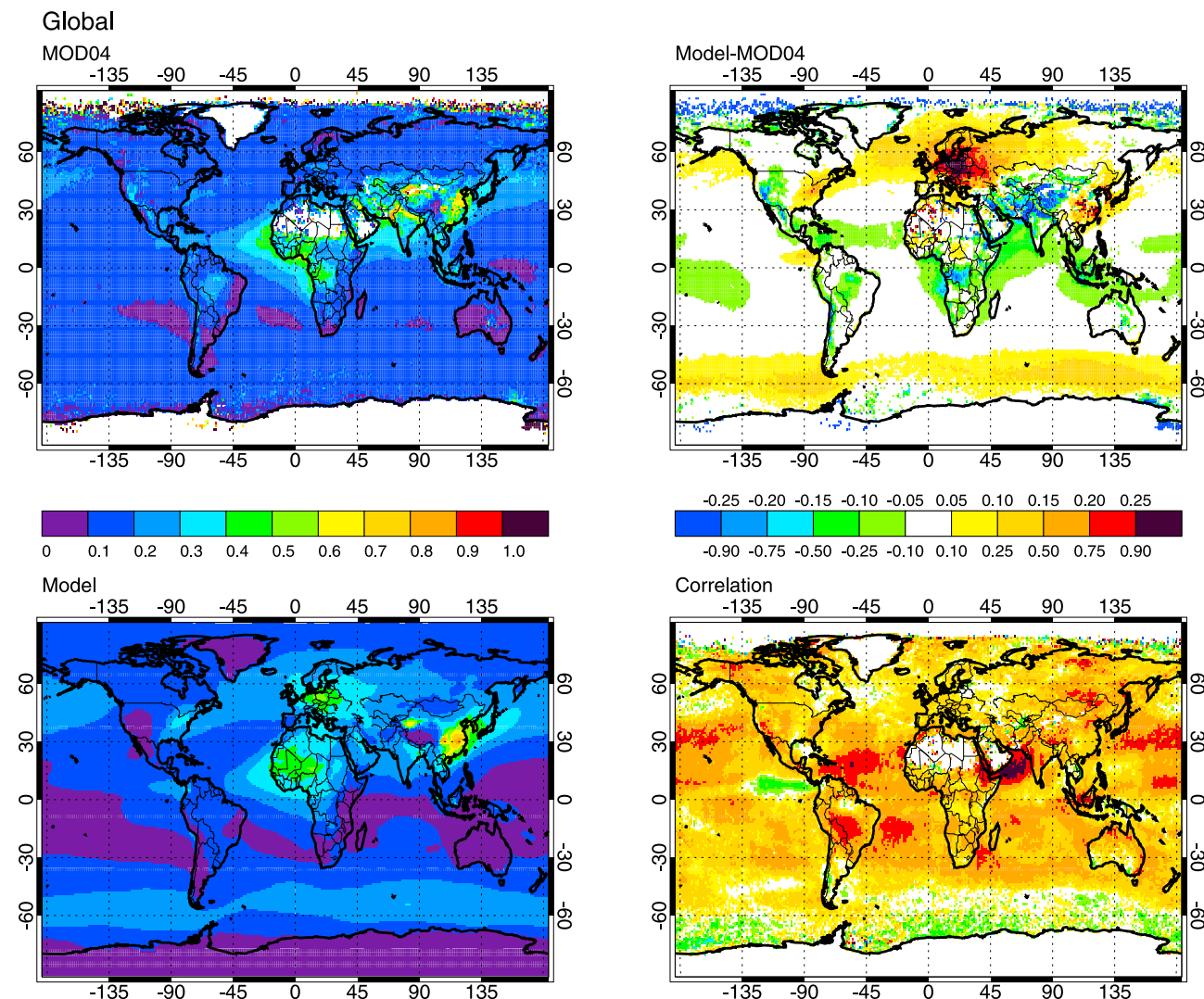


**Figure 9.** Seven year average (2000–2006) of the MODIS Terra (top, left) and the GEOS-4 model (bottom, left) AOT [550 nm] (top, left). Also shown are the difference GEOS-4 – MODIS in the mean AOT (top, right) and the grid-box correlations of the GEOS-4 monthly means against the MODIS monthly means (bottom, right). Results are shown for the unsampled monthly mean of the model compared to the satellite observations.

[55] Over the ocean, the MODIS AOT  $\tau_{550} = 0.16$  and the sampled model AOT  $\tau_{550} = 0.14$ , and the correlation is somewhat poorer ( $r = 0.57$ ) than globally over the land. We graphically show the ocean analysis additionally for only the tropical North Atlantic, the Caribbean, and the Southern Ocean, but the analysis for other ocean regions shown in Figure 11 is summarized as well in Table 4. In the tropical North Atlantic, where the aerosol load is dominated by mineral dust, the model develops a similar magnitude and temporal evolution ( $r = 0.86$ ) to the MODIS observations. For comparison we show the Caribbean basin, which is the receptor of much of that mineral dust and see that the model AOT is considerably less than the observed AOT, suggesting too much removal of dust as it transits the Atlantic. In the Southern Ocean the model AOT is dominated by sea salt aerosols, and despite our reduction of the overall sea salt

burden the model AOT is still about 10% greater than the MODIS observations.

### 3.2.2.3. MISR

[56] We aggregate the MISR Level 2 retrieved AOT at 558 nm to our model grid in a similar fashion to what was done for MODIS. In Figure 12 we also show the MISR monthly mean AOT average over each region (statistics for these and other regions are also tabulated in Table 4). In general, the MISR monthly mean AOT is similar in magnitude and well correlated with the MODIS observations, despite the sampling and weighting differences in the two data sets. The magnitude of the MISR AOT is generally less than the MODIS values, most significantly over land, and especially in North America and Asia. Note that the reduced spatial sampling of MISR relative to MODIS implies that MODIS observes more of the high aerosol events that can

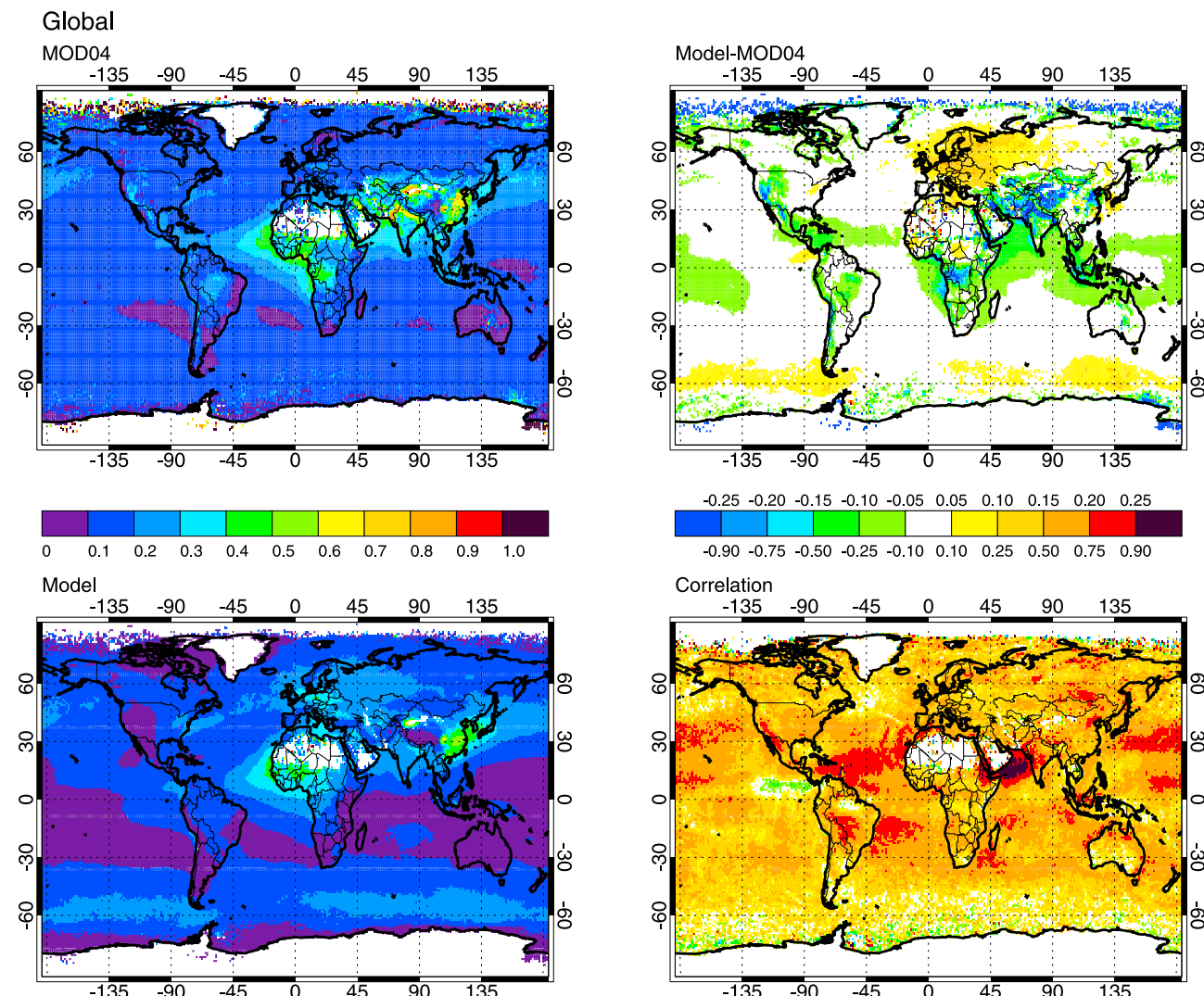


**Figure 10.** As in Figure 9 but for the sampled monthly mean of the model compared to the satellite observations.

dominate the regionally averaged AOT. Over the ocean regions, the correlation of the MISR and MODIS monthly means is always greater than 0.9 except in especially cloud-covered regions (e.g., Northern Ocean, Southern Ocean, and southeastern Pacific) where sampling would be more of a consideration. The correlation of MISR and MODIS is similarly high over the land, except in North Africa ( $r = 0.75$ ), where MISR sees considerably more of the surface than MODIS, and in northern Asia ( $r = 0.72$ ), where MISR has a considerably lower AOT than MODIS.

[57] The comparison of the model to MISR is qualitatively similar to the model versus MODIS results. The notable exception illustrated in Figure 12 is over the western United States, where the MISR AOT is much lower than MODIS and similar in magnitude to the model (MISR AOT is biased low relative to MODIS, as is the model AOT). We note that for the results shown in Figure 12, the model traces are from the model sampled with the MODIS observation statistics. Strictly speaking, the model should be sampled consistently with the MISR observations to form a second set of monthly means for this comparison. We have done

this (not shown) and the results indicate some differences, especially over the high latitudes and bright desert regions (Northern Africa) owing to different sampling statistics of MISR in these regions, but this does not substantially change the conclusions here.

#### 4. Discussion

[58] We showed that the GEOS-4 aerosol emissions and simulation of aerosol lifecycle (burden and loss rates) is generally within the range of the AeroCom suite of models and is similar to the offline GOCART model. The significant differences between GEOS-4 and the offline GOCART relate to scaling of dust and sea salt emissions and differences in biomass burning emissions. The dry removal processes of dust and sea salt seem underestimated in GEOS-4 with respect to GOCART and the AeroCom models. The somewhat longer wet removal lifetime of carbonaceous aerosols in GEOS-4 relative to the AeroCom models may be related to longer conversion time of hydrophobic to hydrophilic modes assumed in GEOS-4. A shorter conver-

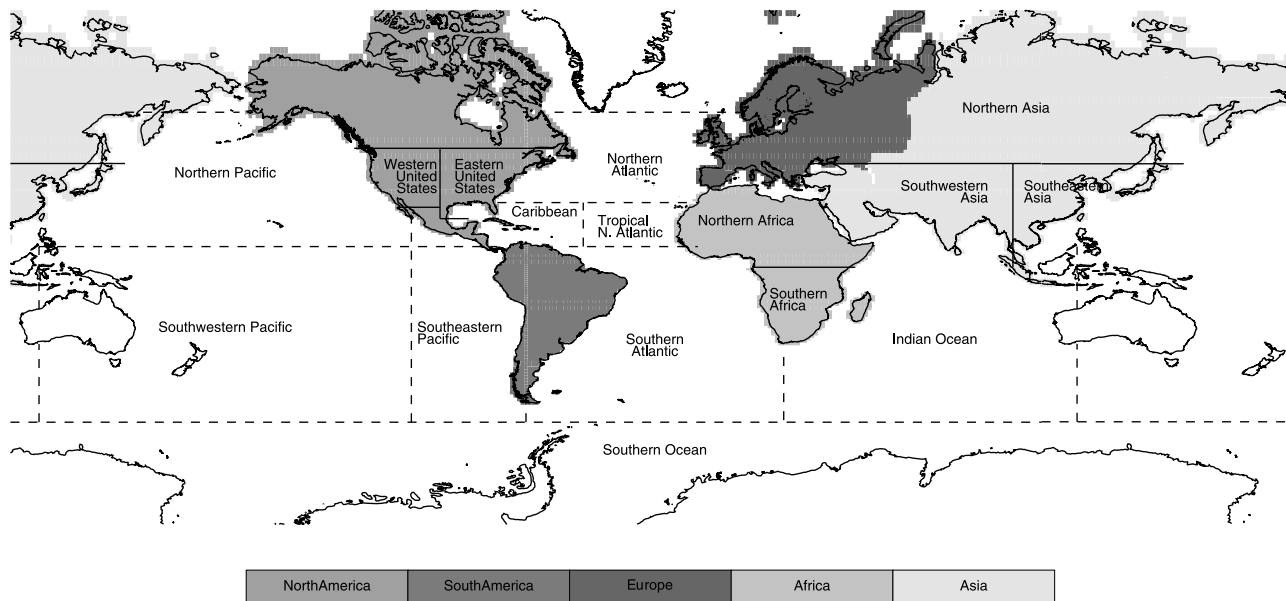


**Figure 11.** Map showing the region definitions used in Figure 12 and Table 4.

sion time to the hydrophilic mode would lead to more rapid wet removal but also might improve the AOT comparison in biomass-burning regions because this will lead to a higher AOT in higher humidity environments. These issues will be the subjects of further work elsewhere.

[59] The remainder of our discussion focuses on the simulated aerosol optical thickness. For all species, the GEOS-4 mass extinction efficiencies assumed are within the range of the AeroCom values. The simulated AOT magnitude is also similar to the offline GOCART and AeroCom model results, except in the cases of sea salt (as discussed above) and sulfate. For sulfate, the simulated AOT is slightly higher than the range of AeroCom models but is similar to GOCART. Likewise, the mass extinction efficiency for sulfate is somewhat greater than the mean of the AeroCom results. The mass extinction efficiency for sulfate is a strong function of environmental humidity, and so differences may arise here because of the humidity values in GEOS-4 relative to other models.

[60] For the remainder of the analysis here we recall that we have reduced the sea salt burden in the model by a factor of two. The simulated AOT is well correlated with the overall AERONET AOT and Angstrom parameter values (Figure 8) and we develop similar seasonal and interannual variability, as illustrated for select AERONET sites representative of different aerosol regimes (Figures 4–7). The model has its lowest skill in AOT ( $s_{\tau} < 0.4$  as in Table 3) at 8 of the 53 sites considered, which are primarily biomass burning influenced sites in South America, southern Africa, and Australia. The model Angstrom parameter is biased low relative to AERONET at all sites and has its lowest skill ( $s_{\alpha} < 0.4$  as in Table 3) at 4 of the 53 sites, 3 of which are dust dominated (Solar Village, Dakar, and Dalanzadgad). The fourth site is Mongu, which is biomass burning dominated; likewise, Dakar and Dalanzadgad have seasonal incursions of influence from biomass burning.

[61] The MODIS and MISR data sets are well correlated with each other (Table 4), with the worst correlations occurring over land in northern Asia and northern Africa and over the ocean in the southeastern Pacific. We would not necessarily expect good correlation over northern Asia and northern Africa because of the prevalence of bright surfaces (deserts and snow in Asia, deserts in Africa) that particularly hamper the MODIS retrievals. It is not immediately clear why the correlation is less good over the southeastern Pacific, except that in our analysis this is a relatively small region that is frequently cloud obscured. Over ocean, the bias between MODIS and MISR monthly mean AOT is 0.015 or smaller. Over land, the biases are generally greater, with MODIS having a higher AOT in all regions except northern Africa, where few retrievals are ever attempted. The bias is the largest over the western United States and in southeastern and western Asia. A recent study comparing MODIS land retrievals and AERONET observations in these regions (R. C. Levy, L. A. Remer, R. G. Kleidman, S. Mattoo, C. Ichoku, and T. F. Eck, Global evaluation of the Collection 5 MODIS aerosol products over land, submitted to *Atmospheric Chemistry and Physics*, 2010) generally found that MODIS AOT is high relative to AERONET, which is attributed to poorly characterized retrievals over marginally bright surfaces. This high bias in the MODIS AOT explains the better agreement of the model with MISR and AERONET in these regions.

[62] Comparing the sampled and unsampled model AOT to one another in Table 4 and Figures 10–12 reveals that the regional AOT is greater in the unsampled model case in all regions considered except the tropical North Atlantic. In general, the unsampled model has greater overall skill at reproducing the MODIS AOT observations over land, while the sampled model has better skill over the ocean (Table 4). Over land, the unsampled model compares better to MODIS in biomass-burning areas (in northern and southern Africa, South America, and southern and western Asia), where the

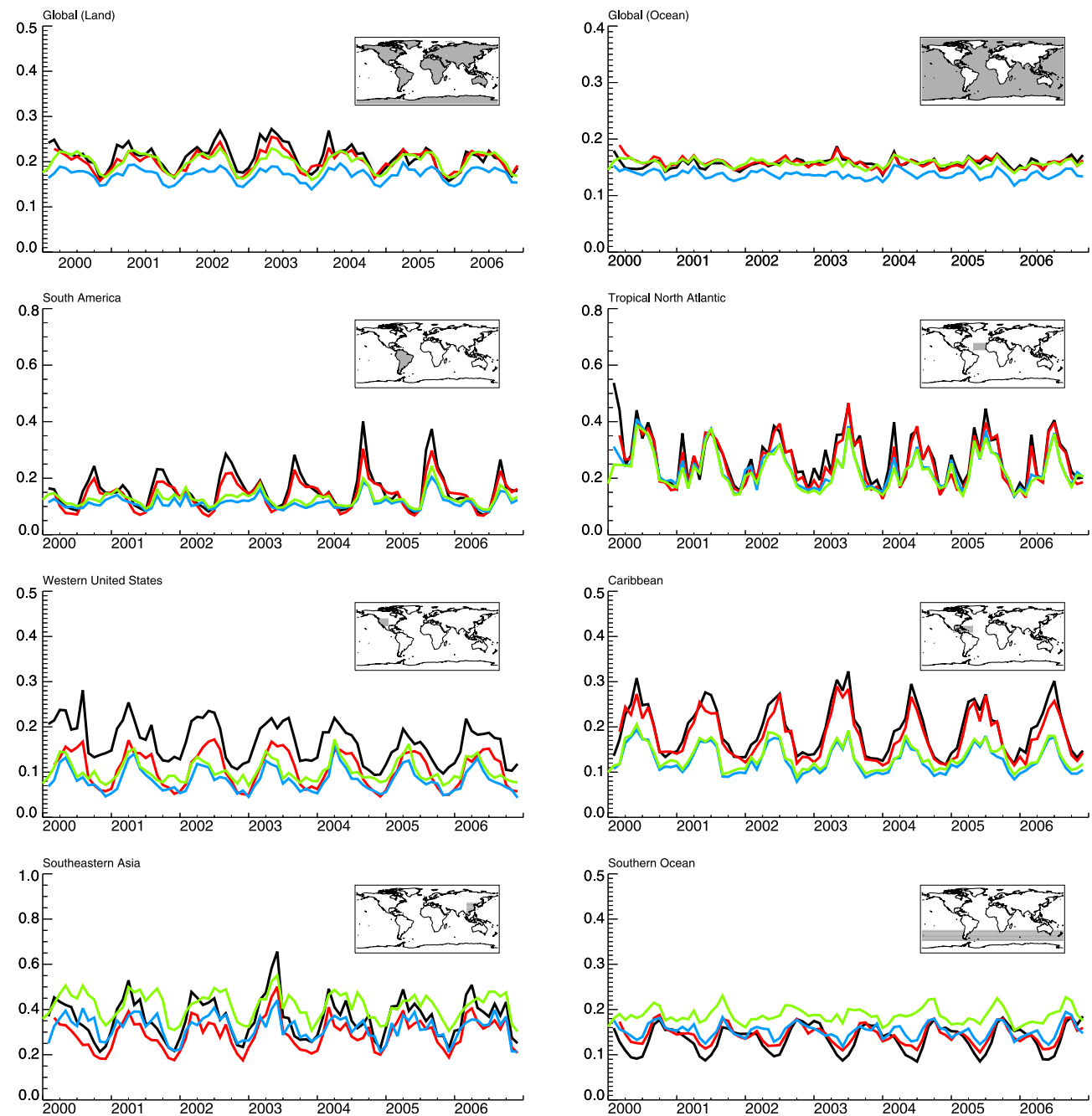


**Figure 12.** Comparison of the monthly means of the model and satellite observations of AOT [550 nm] for various regions. Shown are the MODIS Terra (black), MISR (red), sampled GEOS-4 (blue), and unsampled GEOS-4 model (green).

sampled model AOT is considerably lower than the satellite observations. Over ocean, the unsampled model compares more favorably in the Indian Ocean, southwest Pacific, and North and South Atlantic regions.

[63] We consider three possible explanations for differences in the sampled and unsampled model mean AOT. First, we consider a diurnal effect: in constructing the unsampled model comparison we are using the AOT from all four model synoptic output times (0, 6, 12, and 18 UTC) throughout the month and not simply at the satellite overpass time, and because of diurnal variations in aerosol

loading and optical properties (e.g., response to environmental humidity) we might find the explanation for the difference. To investigate this case we constructed four additional unsampled model monthly mean analyses, one each averaging the model output only at 0, 6, 12, and 18 UTC (for brevity, results not shown here). While the greatest differences between the unsampled and sampled model regional AOT (Table 4) is as much as 40% over land and 20% over the ocean (depending on the region), the difference between any of the four synoptic unsampled and “all-times” unsampled monthly regional AOT is only about

**Table 4.** Statistics for the Monthly Means of the MODIS Terra, MISR, and GEOS-4 AOT for Land (left) and Ocean (right) Regions Indicated in Figure 11<sup>a</sup>

Global (Land, 180°W–180°E, 90°S–90°N)				Global (Ocean, 180°W–180°E, 90°S–90°N)					
	$\langle \tau_{550} \rangle$	<i>r</i>	<i>b</i>	Skill		$\langle \tau_{550} \rangle$	<i>r</i>	<i>b</i>	Skill
MODIS	0.210				MODIS	0.157			
MISR	0.202	0.899	-0.008	0.905	MISR	0.158	0.720	0.001	0.858
G4	0.171	0.747	-0.039	0.612	G4	0.137	0.570	-0.020	0.759
G4uns	0.199	0.755	-0.011	0.800	G4uns	0.158	0.533	0	0.699
North America				Tropical N. Atlantic (50°W–0°W, 10°N–30°N)					
	$\langle \tau_{550} \rangle$	<i>r</i>	<i>b</i>	Skill		$\langle \tau_{550} \rangle$	<i>r</i>	<i>b</i>	Skill
MODIS	0.150				MODIS	0.273			
MISR	0.125	0.964	-0.025	0.967	MISR	0.254	0.959	-0.015	0.979
G4	0.113	0.764	-0.037	0.587	G4	0.235	0.856	-0.038	0.853
G4uns	0.147	0.783	-0.003	0.471	G4uns	0.226	0.802	-0.046	0.823
South America				Caribbean (100°W–50°W, 10°N–30°N)					
	$\langle \tau_{550} \rangle$	<i>r</i>	<i>b</i>	Skill		$\langle \tau_{550} \rangle$	<i>r</i>	<i>b</i>	Skill
MODIS	0.158				MODIS	0.195			
MISR	0.143	0.953	-0.015	0.927	MISR	0.182	0.973	-0.014	0.978
G4	0.115	0.727	-0.043	0.355	G4	0.127	0.914	-0.068	0.680
G4uns	0.128	0.757	-0.029	0.443	G4uns	0.135	0.885	-0.061	0.642
Eastern United States				South Atlantic (70°W–20°E, 60°S–10°N)					
	$\langle \tau_{550} \rangle$	<i>r</i>	<i>b</i>	Skill		$\langle \tau_{550} \rangle$	<i>r</i>	<i>b</i>	Skill
MODIS	0.148				MODIS	0.204			
MISR	0.140	0.974	-0.008	0.949	MISR	0.200	0.957	-0.004	0.967
G4	0.158	0.720	0.010	0.650	G4	0.165	0.583	-0.039	0.687
G4uns	0.221	0.683	0.073	0.679	G4uns	0.170	0.550	-0.034	0.707
Western United States				North Atlantic (80°W–0°W, 30°N–60°N)					
	$\langle \tau_{550} \rangle$	<i>r</i>	<i>b</i>	Skill		$\langle \tau_{550} \rangle$	<i>r</i>	<i>b</i>	Skill
MODIS	0.167				MODIS	0.173			
MISR	0.107	0.882	-0.060	0.930	MISR	0.178	0.909	0.007	0.912
G4	0.083	0.730	-0.084	0.665	G4	0.183	0.554	0.010	0.620
G4uns	0.102	0.669	-0.065	0.586	G4uns	0.220	0.434	0.047	0.649
Southern Africa				Northern Ocean (180°W–180°E, 60°N–90°N)					
	$\langle \tau_{550} \rangle$	<i>r</i>	<i>b</i>	Skill		$\langle \tau_{550} \rangle$	<i>r</i>	<i>b</i>	Skill
MODIS	0.200				MODIS	0.153			
MISR	0.196	0.960	-0.004	0.962	MISR	0.157	0.882	0.004	0.895
G4	0.121	0.415	-0.079	0.536	G4	0.159	0.348	0.005	0.659
G4uns	0.131	0.375	-0.069	0.583	G4uns	0.165	0.340	0.012	0.475
Northern Africa				Southern Ocean (180°W–180°E, 60°S–30°S)					
	$\langle \tau_{550} \rangle$	<i>r</i>	<i>b</i>	Skill		$\langle \tau_{550} \rangle$	<i>r</i>	<i>b</i>	Skill
MODIS	0.314				MODIS	0.136			
MISR	0.329	0.727	0.018	0.859	MISR	0.144	0.864	0.008	0.823
G4	0.282	0.555	-0.032	0.455	G4	0.152	0.708	0.016	0.615
G4uns	0.325	0.426	0.011	0.635	G4uns	0.187	0.263	0.051	0.463
Europe				Indian Ocean (20°E – 120°E, 30°S–30°N)					
	$\langle \tau_{550} \rangle$	<i>r</i>	<i>b</i>	Skill		$\langle \tau_{550} \rangle$	<i>r</i>	<i>b</i>	Skill
MODIS	0.151				MODIS	0.176			
MISR	0.133	0.915	-0.018	0.871	MISR	0.171	0.920	-0.005	0.957
G4	0.240	0.665	0.089	0.831	G4	0.113	0.861	-0.063	0.792
G4uns	0.316	0.576	0.165	0.762	G4uns	0.122	0.824	-0.053	0.843
Northern Asia				Northern Pacific (120°E–110°W, 10°N–60°N)					
	$\langle \tau_{550} \rangle$	<i>r</i>	<i>b</i>	Skill		$\langle \tau_{550} \rangle$	<i>r</i>	<i>b</i>	Skill
MODIS	0.192				MODIS	0.172			
MISR	0.125	0.682	-0.066	0.755	MISR	0.171	0.920	-0.005	0.957
G4	0.173	0.591	-0.020	0.594	G4	0.156	0.863	-0.016	0.889
G4uns	0.201	0.638	0.008	0.447	G4uns	0.181	0.807	0.009	0.883

**Table 4.** (continued)

Southern Asia				SE Pacific (110°W–70°W, 60°S–10°N)					
	$\langle \tau_{550} \rangle$	r	b	Skill		$\langle \tau_{550} \rangle$	r	b	Skill
MODIS	0.363				MODIS	0.124			
MISR	0.292	0.978	-0.071	0.928	MISR	0.136	0.629	0.011	0.726
G4	0.321	0.738	-0.042	0.685	G4	0.126	0.467	0.001	0.730
G4uns	0.419	0.702	0.056	0.734	G4uns	0.134	0.47	0.01	0.712
Western Asia				SW Pacific (120°E–110°W, 60°S–10°N)					
	$\langle \tau_{550} \rangle$	r	b	Skill		$\langle \tau_{550} \rangle$	r	b	Skill
MODIS	0.297				MODIS	0.152			
MISR	0.234	0.955	-0.063	0.967	MISR	0.163	0.881	0.011	0.891
G4	0.198	0.848	-0.099	0.756	G4	0.093	0.804	-0.059	0.642
G4uns	0.235	0.887	-0.062	0.858	G4uns	0.105	0.709	-0.048	0.687

<sup>a</sup>Note. Where a continent name is given, the entire continent (as defined by the shading in Figure 11) is used in the average. For ocean regions we also give the latitude and longitude of the bounding boxes used (ocean grid points only) in the averaging. For each region we show the monthly mean AOT ( $\langle \tau_{550} \rangle$ ), correlation coefficient (r), bias (b), and skill, where the correlation coefficient, bias, and skill are relative to the MODIS observations. Two instances of the model are shown: our sampled model monthly mean statistics (G4) and the unsampled model monthly mean statistics (G4uns).

10% in South America and southern Africa (i.e., biomass burning regions) and is smaller elsewhere.

[64] We note here that the swath approach to constructing the monthly mean described previously yields essentially identical results to the unsampled approach. Just as there were no real variations in the model monthly mean AOT with the 0, 6, 12, and 18 UTC model output were separately compared to one another and to the “all-times” unsampled monthly mean, the swath approach amounts to sampling the model at the same local time at all grid boxes (i.e., the MODIS Terra daytime overpass at the equator is approximately 10:30 AM local time) and so is really just a variation on the diurnal sampling described above. Because the results for the swath approach are so similar to the unsampled approach we neglect consideration of it in the remaining discussion. These results imply the diurnal variation in AOT is negligible to the monthly mean.

[65] A second possible explanation is in the seasonal frequency of observation. Since MODIS requires sunlight to make aerosol retrievals, as sunlight retreats at high latitudes in the winter there are fewer retrievals made, and a seasonal shift in the northernmost retrievals is apparent as monthly mean plots are compared. In a similar fashion, MODIS does not make retrievals over the bright snow- or ice-covered surfaces that generally follow the same seasonal pattern as sunlight. We constructed again the monthly analysis for the unsampled model separately for each of our four synoptic output times, this time, however, masking the individual monthly means so that we only retained grid boxes that were present in the monthly mean of the satellite observations. The results of this comparison (also not shown) were nearly identical to the synoptic unsampled monthly regional AOT described above.

[66] The explanation then for the difference between the unsampled and sampled model mean AOT is thus in spatial sampling within an orbital swath of the MODIS instrument. In other words, it is important to the monthly mean where MODIS does and does not make retrievals on a particular orbit. Since MODIS does not retrieve aerosols in cloudy conditions, for example, its retrieved AOT must be con-

sidered biased toward less humid environments. We illustrate this point in Figure 13, which shows the model daily average AOT and the model and MODIS cloud fraction on 5 June 2000. Our choice of date here is arbitrary, merely to illustrate the point. On the left we show the simple model daily average AOT (top) and the same data masked to exclude locations MODIS Terra did not make an aerosol retrieval (bottom). On the right we show the model daily average cloud fraction (top) and the MODIS cloud fraction (bottom). Evaluating the model cloud fraction in the context of the MODIS observations is beyond the scope of this study, but there is a visible correlation between the high cloud fraction features in the model and MODIS data, as well as between high model cloud fraction and high model AOT. While we have not performed this analysis for all days aggregated in Figures 9 and 10, we can with some confidence state that the difference between the sampled and unsampled monthly mean model AOT is due to this feature of the sampled model AOT being biased against high cloud fraction. Because MODIS does not retrieve AOT in high-cloud-fraction environments, the sampled model AOT comparison to MODIS observations seems the more appropriate comparison to make.

[67] Overall, there is consistency in our interpretation of the model AOT in terms of the AERONET and satellite data sets. For all land regions except Europe and the eastern United States the model is biased low in AOT relative to MODIS (Table 4 and Figure 10), consistent with the overall comparison to AERONET. The high biases in Europe and the eastern United States are explained in terms of the relatively high sulfate AOT magnitude, which is the dominant component of AOT in these regions. The worst model skill over land relative to MODIS is in South America, where we have underestimated biomass burning emissions; we have a large low bias relative to MODIS in southern Africa for the same basic reason. The model’s lowest biases relative to MODIS are in the western United States and western Asia, but we have pointed out that MODIS is likely biased high in these regions and that the model agrees better with MISR as a result.

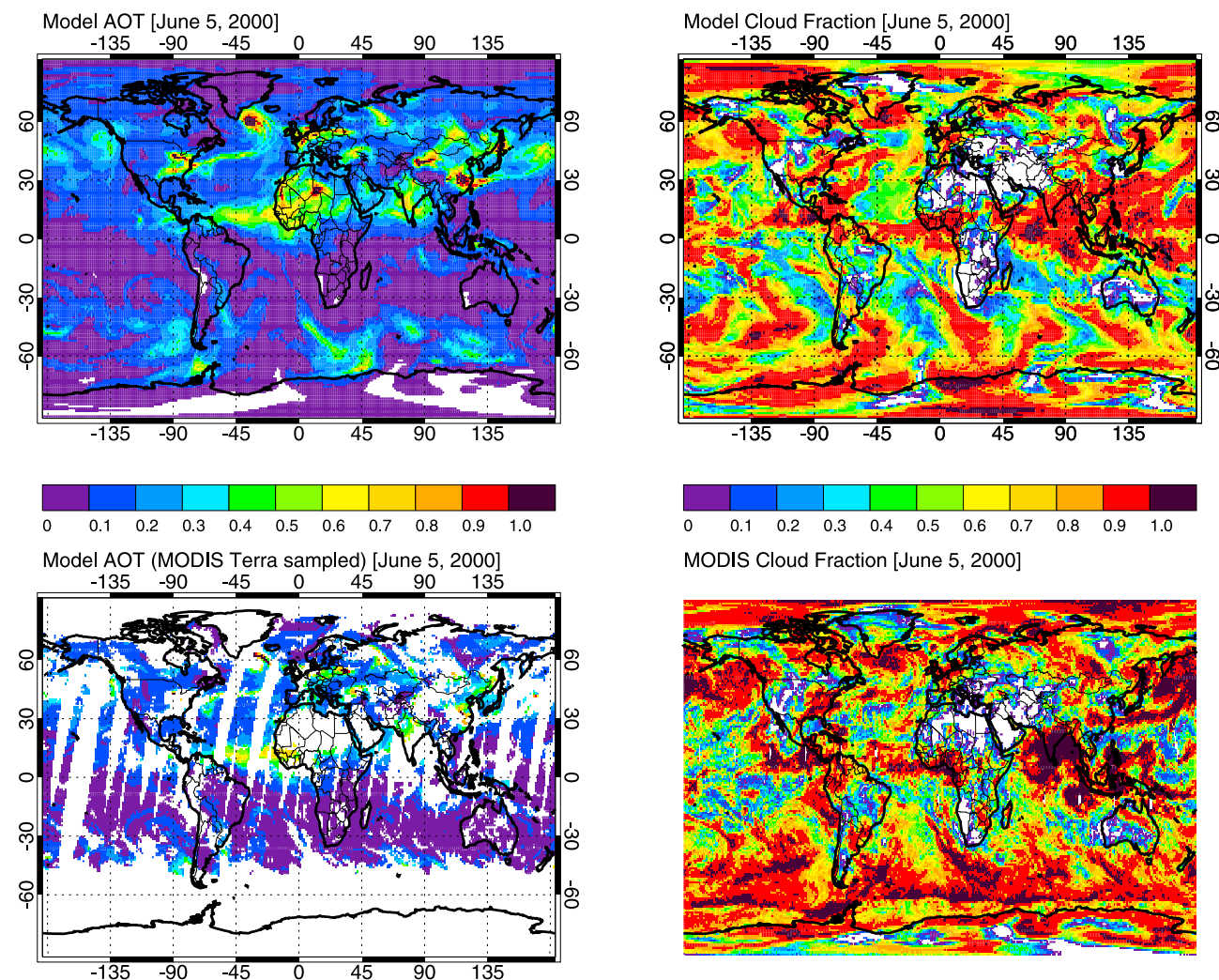


**Figure 13.** The unsampled daily average model AOT (top, left) and the sampled model AOT (bottom, left) on 5 June 5 2000. Also shown are the model cloud fraction (top, right) and the MODIS Terra cloud fraction (bottom, right).

[68] Over the ocean the picture is somewhat different, with a clear positive bias remaining in the model at high southern latitudes (Figure 10). As discussed earlier, the model has a high sea salt aerosol burden relative to other models, and even after reduction of the burden by a factor of 2 the GEOS-4 AOT remains somewhat high. In other ocean regions where sea salt is not the dominant component, however, there tends to be a low bias in the model AOT relative to MODIS. West of southern Africa, for example, where biomass burning is an important player, we see the result of too low export of biomass burning aerosol into this region. Likewise we see too little export of dust from the Sahara Desert into the tropical North Atlantic and Caribbean regions, and even a hint of the dust plume traveling too far to the south. We also see a low bias in regions influenced by complicated mixtures of dust, pollution, and biomass burning aerosols (Indian Ocean and Indonesian ocean region). This analysis suggests, for example, that the removal of dust downwind of the Sahara is too efficient in our model because although we have the seasonal variability in AOT in the

Caribbean we underestimate the magnitude of the peak AOT (in June and July) by almost a factor of 2 (Figure 12).

## 5. Conclusions

[69] We have implemented a version of the GOCART aerosol module online in the GEOS-4 atmospheric general circulation model and data assimilation system. The model has been used to simulate the global distributions of aerosols for the period 2000–2006. The emissions, burdens, and lifetimes of aerosols in GEOS-4 are within the range of similar aerosol models that participated in the AeroCom model intercomparison studies and are similar to the results of the offline GOCART model. The exception to the above statement is that the modeled sea salt aerosol burden is about three times greater than the mean of the AeroCom models and about twice as great as the burden developed in the offline GOCART model. We attribute the excessive sea salt burden to inefficient removal through sedimentation. To

a lesser extent this is also a problem in the treatment of dust aerosols in our model.

[70] For all species in the model, the aerosol mass extinction efficiency used is within the range of the AeroCom results. For all species except sea salt and sulfate the model AOT is also within the range of the AeroCom results. For sea salt, the AOT is greater than the mean of the AeroCom results by nearly a factor of 3, consistent with the high sea salt burden discussed above. The sulfate AOT in the model is about 60% greater than the mean of the AeroCom results but is similar in magnitude to the offline GOCART model and is only 5% greater than the highest sulfate AOT of the AeroCom models.

[71] The model total AOT exhibits similar regional and seasonal variability to observations from the AERONET ground-based sun photometers and the space-based MODIS and MISR instruments. Additionally, the model has similar seasonal variability and magnitude in the simulated Angstrom parameter as the AERONET observations at most sites. Compared to AERONET, however, the model AOT and Angstrom parameter are overall biased low, with the model AOT being underestimated especially where the observed AOT value is high. The model AOT is generally low in regions primarily influenced by biomass burning, pointing to errors in emissions used to drive the model and possibly to errors in aging of smoke aerosols from their hydrophobic to hydrophilic modes. This is also the case with the offline GOCART model [Chin *et al.*, 2009b]. In contrast, the model AOT is biased high relative to the observations in primarily sulfate-dominated regions of the U.S. east coast and Europe. The best agreement in both the magnitude and variability of the AOT between the model and observations is immediately downwind of the Saharan dust plume. Fidelity between the model over ocean AOT and satellite AOT is greatly improved by reducing the model sea salt burden by a factor of 2.

[72] The above results point out strengths and limitations in current model evaluation strategies. With global constraints on AOT from satellite data sets, aerosol models are frequently able to match the observations [e.g., Kinne *et al.*, 2006]. The pathway to making that match, however, is less well constrained. As indicated in this paper and the AeroCom results [Textor *et al.*, 2006], for example, differences in the simulated aerosol lifetimes among models can be quite large. We point out that aerosol lifetime and mass are relatively unconstrained on the global scale. This requires a deeper level of analysis and suggests new requirements for next generation space-based observations to provide greater information about aerosol composition.

[73] Additionally, we considered various strategies for comparing the model AOT to satellite monthly mean AOT. We find that the agreement in the comparison is significantly affected by the choice of sampling strategy. The model monthly mean AOT is generally higher if it is computed as the simple mean of all model output relative to the mean computed by first sampling the model at times and locations of satellite AOT retrievals. The differences between the unsampled and sampled monthly mean AOT seems not to result from diurnal variability in either the simulated aerosol load or optical properties but rather to be related to sampling biases introduced because the satellite only observes AOT under clear-sky conditions. Although

there remain biases in the model itself due to errors in emissions and aerosol processes, this analysis suggests a need for model studies to consider these sampling issues in model-data comparisons. We argue here that the sampled model comparison is the more appropriate one to make.

[74] These results provide a foundation for future online studies of global aerosol distributions in the GEOS model. The next generation GEOS version 5 (GEOS-5) model permits investigation of the aerosol direct and semidirect radiative effects through interaction of aerosol fields and the model's radiation package. Additionally, the GEOS chemistry-climate model [Pawson *et al.*, 2008] has implemented stratospheric and (soon) tropospheric chemistry modules into the same GEOS-5 framework that incorporates the online GOCART, which will permit interaction between aerosols and atmospheric chemistry. Future work will also emphasize addressing weaknesses found in the current model, including the lifecycle of sea salt aerosols, biomass-burning aerosol sources, and the treatment of aerosol humidification and subsequent impact on aerosol optical properties.

[75] **Acknowledgments.** We acknowledge the valuable insights to two anonymous reviewers. We thank Huisheng Bian for providing the oxidant fields used for sulfate chemistry in this study. Brent Holben leads the AERONET program and provided access to that data set. Ralph Kahn and Cynthia Randles provided valuable comments on early drafts of this paper. This work was supported by a grant from the NASA Modeling, Analysis, and Prediction program, with Don Anderson acting as the technical director.

## References

- Abdou, W., et al. (2005), Comparison of coincident multiangle imaging spectroradiometer and moderate resolution imaging spectroradiometer aerosol optical depths over land and ocean scenes containing aerosol robotic network sites, *J. Geophys. Res.*, 110(D10), D10S07, doi:10.1029/2004JD004693.
- Albrecht, B. (1989), Aerosols, cloud microphysics, and fractional cloudiness, *Science*, 245(4923), 1227–1230.
- Andreae, M., and P. Merlet (2001), Emission of trace gases and aerosols from biomass burning, *Global Biogeochem. Cy.*, 15(4), 955–966.
- Atwater, M. (1970), Planetary albedo changes due to aerosols, *Science*, 170(3953), 64–66.
- Bauer, S., et al. (2008), MATRIX (Multiconfiguration Aerosol TRacker of mIXing state): An aerosol microphysical module for global atmospheric models, *Atmos. Chem. Phys.*, 8(20), 6003–6035.
- Benedetti, A., et al. (2009), Aerosol analysis and forecast in the European centre for medium-range weather forecasts integrated forecast system: 2. Data assimilation, *J. Geophys. Res.*, 114, D13205, doi:10.1029/2008JD011115.
- Bertschi, I., D. Jaffe, L. Jaegle, H. Price, and J. Dennison (2004), PHOBEA/ITCT 2002 airborne observations of transpacific transport of ozone, CO, volatile organic compounds, and aerosols to the northeast Pacific: Impacts of Asian anthropogenic and Siberian boreal fire emissions, *J. Geophys. Res.*, 109(D23), D23S12, doi:10.1029/2003JD004328.
- Bey, I., et al. (2001), Global modeling of tropospheric chemistry with assimilated meteorology: Model description and evaluation, *J. Geophys. Res.*, 106(D19), 23,073–23,095.
- Bloom, S., A. da Silva, and D. Dee (2005), Documentation and validation of the Goddard Earth Observing System (GEOS) data assimilation system—version 4, 1–187 pp.
- Bonan, G., et al. (2002), The land surface climatology of the community land model coupled to the NCAR community climate model, *J. Clim.*, 15(22), 3123–3149.
- Carn, S. A., A. J. Krueger, G. S. J. Bluth, S. J. Schaefer, N. A. Krotkov, I. M. Watson, and S. Datta (2003), Volcanic eruption detection by the total ozone mapping spectrometer (TOMS) instruments: A 22-year record of sulfur dioxide and ash emissions, in *Volcanic Degassing*, Special Publication of the Geological Society of London No. 213, edited by C. Oppenheimer, D. M. Pyle, and J. Barclay, pp. 177–202, Geological Society, London, UK.

- Charlson, R. J., and M. J. Pilat (1969), Climate: The influence of aerosols, *J. App. Met.*, 8, 1001–1002.
- Chin, M., R. Rood, S. Lin, J. Muller, and A. Thompson (2000), Atmospheric sulfur cycle simulated in the global model GOCART: Model description and global properties, *J. Geophys. Res.*, 105(D20), 24,671–24,687.
- Chin, M., et al. (2002), Tropospheric aerosol optical thickness from the GOCART model and comparisons with satellite and Sun photometer measurements, *J. Atmos. Sci.*, 59(3), 461–483.
- Chin, M., et al. (2003), A global aerosol model forecast for the ACE-Asia field experiment, *J. Geophys. Res.*, 108(D23), 8654, doi:10.1029/2003JD003642.
- Chin, M., A. Chu, R. Levy, L. Remer, Y. Kaufman, B. Holben, T. Eck, P. Ginoux, and Q. Gao (2004), Aerosol distribution in the Northern Hemisphere during ACE-Asia: Results from global model, satellite observations, and Sun photometer measurements, *J. Geophys. Res.*, 109(D23), D23S90, doi:10.1029/2004JD004829.
- Chin, M., T. Diehl, P. Ginoux, and W. Malm (2007), Intercontinental transport of pollution and dust aerosols: implications for regional air quality, *Atmos. Chem. Phys.*, 7(21), 5501–5517.
- Chin, M., et al. (2009a), Atmospheric aerosol properties and climate impacts: Synthesis and assessment product 2.3. Report by the U.S. Climate Change Science Program and the Subcommittee on Global Change Research (<http://www.gcrio.org/orders>), 116 pp.
- Chin, M., et al. (2009b), Light absorption by pollution, dust, and biomass burning aerosols: a global model study and evaluation with AERONET measurements, *Ann. Geophys.*, 27, 3439–3464.
- Colarco, P., M. Schoeberl, B. Doddridge, L. Marufu, O. Torres, and E. Welton (2004), Transport of smoke from Canadian forest fires to the surface near Washington, D.C.: Injection height, entrainment, and optical properties, *J. Geophys. Res.*, 109, D06203, doi:10.1029/2003JD004248.
- Colarco, P., O. Toon, and B. Holben (2003), Saharan dust transport to the Caribbean during PRIDE: 1. Influence of dust sources and removal mechanisms on the timing and magnitude of downwind aerosol optical depth events from simulations of in situ and remote sensing observations, *J. Geophys. Res.*, 108(D19), 8589, doi:10.1029/2002JD002658.
- Colarco, P., O. Toon, O. Torres, and P. Rasch (2002), Determining the UV imaginary index of refraction of Saharan dust particles from total ozone mapping spectrometer data using a three-dimensional model of dust transport, *J. Geophys. Res.*, 107(D16), 4289, doi:10.1029/2001JD000903.
- Collins, W., P. Rasch, B. Eaton, B. Khattatov, J. Lamarque, and C. Zender (2001), Simulating aerosols using a chemical transport model with assimilation of satellite aerosol retrievals: Methodology for INDOEX, *J. Geophys. Res.*, 106(D7), 7313–7336.
- Cooke, W., C. Lioussse, H. Cachier, and J. Feichter (1999), Construction of a 1 degrees × 1 degrees fossil fuel emission data set for carbonaceous aerosol and implementation and radiative impact in the ECHAM4 model, *J. Geophys. Res.*, 104(D18), 22,137–22,162.
- Dentener, F., et al. (2006), Emissions of primary aerosol and precursor gases in the years 2000 and 1750 prescribed data-sets for AeroCom, *Atmos. Chem. Phys.*, 6, 4321–4344.
- Diner, D., et al. (2004), PARAGON: An integrated approach for characterizing aerosol climate impacts and environmental interactions, *Bull. Am. Meteorol. Soc.*, 85(10), 1491–1501.
- Dubovik, O., et al. (2002), Variability of absorption and optical properties of key aerosol types observed in worldwide locations, *J. Atmos. Sci.*, 59(3), 590–608.
- Gerber, H. E. (1985), Relative-humidity parameterization of the Navy aerosol model (NAM), NRL Rep. 8956, Naval Res. Lab., Washington, D. C.
- Ginoux, P., et al. (2001), Sources and distributions of dust aerosols simulated with the GOCART model, *J. Geophys. Res.*, 106(D17), 20,255–20,273.
- Goloub, P., D. Tanré, J. Deuze, M. Herman, A. Marchand, and F. Breon (1999), Validation of the first algorithm applied for deriving the aerosol properties over the ocean using the POLDER ADEOS measurements, *IEEE Trans. Geosci. and Remote Sens.*, 37(3), 1586–1596.
- Gong, S. (2003), A parameterization of sea-salt aerosol source function for sub- and super-micron particles, *Global Biogeochem. Cy.*, 17(4), 1097.
- Gong, S., L. Barrie, and J. Blanchet (1997), Modeling sea-salt aerosols in the atmosphere: 1. Model development, *J. Geophys. Res.*, 102(D3), 3805–3818.
- Grell, G., et al. (2005), Fully coupled “online” chemistry within the WRF model, *Atmos. Environ.*, 39(37), 6957–6975.
- Gunn, R., and B. Phillips (1957), An experimental investigation of the effect of air pollution on the initiation of rain, *J. Atmos. Sci.*, 14(3), 272–280.
- Heald, C., et al. (2006), Concentrations and sources of organic carbon aerosols in the free troposphere over North America, *J. Geophys. Res.*, 111, D23S47, doi:10.1029/2006JD007705.
- Herman, J., P. Bhartia, O. Torres, C. Hsu, C. Seftor, and E. Celarier (1997), Global distribution of UV-absorbing aerosols from Nimbus 7/TOMS data, *J. Geophys. Res.*, 102(D14), 16,911–16,922.
- Holben, B., et al. (1998), AERONET: A federated instrument network and data archive for aerosol characterization, *Remote Sens. of Environ.*, 66(1), 1–16.
- Holben, B., et al. (2001), An emerging ground-based aerosol climatology: Aerosol optical depth from AERONET, *J. Geophys. Res.*, 106(D11), 12,067–12,097.
- Intergovernmental Panel on Climate Change (2007), Climate change 2007: The physical science basis, Contribution of Working Group I to the Fourth Assessment Report of the Intergovernmental Panel on Climate Change, edited by S. Solomon et al., 996 pp., Cambridge University Press, Cambridge, United Kingdom and New York, NY, USA.
- Jacobson, M. (1997a), Development and application of a new air pollution modeling system: 3. Aerosol-phase simulations, *Atmos. Environ.*, 31(4), 587–608.
- Jacobson, M. (1997b), Development and application of a new air pollution modeling system.2. Aerosol module structure and design, *Atmos. Environ.*, 31(2), 131–144.
- Jacobson, M. (2001), Strong radiative heating due to the mixing state of black carbon in atmospheric aerosols, *Nature*, 409(6821), 695–697.
- Jaffe, D., I. McKendry, T. Anderson, and H. Price (2003), Six ‘new’ episodes of trans-Pacific transport of air pollutants, *Atmos. Environ.*, 37(3), 391–404.
- Kahn, R., B. Gaitley, J. Martonchik, D. Diner, K. Crean, and B. Holben (2005), Multiangle Imaging Spectroradiometer (MISR) global aerosol optical depth validation based on 2 years of coincident Aerosol Robotic Network (AERONET) observations, *J. Geophys. Res.*, 110(D10), D10S04, doi:10.1029/2004JD004706.
- Kahn, R., et al. (2008), Wildfire smoke injection heights: Two perspectives from space, *Geophys. Res. Lett.*, 35(4), L04809, doi:10.1029/2007GL032165.
- Kaufman, Y., D. Tanré, O. Dubovik, A. Karniel, and L. Remer (2001), Absorption of sunlight by dust as inferred from satellite and ground-based remote sensing, *Geophys. Res. Lett.*, 28(8), 1479–1482.
- Kaufman, Y., D. Tanré, and O. Boucher (2002), A satellite view of aerosols in the climate system, *Nature*, 419(6903), 215–223.
- Kiehl, J. T., J. J. Hack, G. B. Bonan, B. A. Boville, B. P. Briegleb, D. L. Williamson, and P. J. Rasch (1996), Description of the NCAR Community Climate Model (CCM3). NCAR Technical Note, NCAR/TN-420+STR, Boulder, CO, 152 pp.
- King, M., Y. Kaufman, D. Tanré, and T. Nakajima (1999), Remote sensing of tropospheric aerosols from space: Past, present, and future, *Bull. Am. Meteorol. Soc.*, 80(11), 2229–2259.
- Kinne, S., et al. (2006), An AeroCom initial assessment - optical properties in aerosol component modules of global models, *Atmos. Chem. Phys.*, 6, 1815–1834.
- Kinnison, D., et al. (2001), The global modeling initiative assessment model: Application to high-speed civil transport perturbation, *J. Geophys. Res.*, 106(D2), 1693–1711.
- Koch, D. (2001), Transport and direct radiative forcing of carbonaceous and sulfate aerosols in the GISS GCM, *J. Geophys. Res.*, 106(D17), 20,311–20,332.
- Koepke, P., M. Hell, I. Schult, and E. P. Shettle (1997), Global aerosol data set, Tech. Rep. 243, Max-Planck Institute, 44 pp.
- Levy, R., L. Remer, and O. Dubovik (2007a), Global aerosol optical properties and application to moderate resolution imaging spectroradiometer aerosol retrieval over land, *J. Geophys. Res.*, 112, D13210, doi:10.1029/2006JD007815.
- Levy, R., L. Remer, S. Mattoe, E. Vermote, and Y. Kaufman (2007b), Second-generation operational algorithm: Retrieval of aerosol properties over land from inversion of moderate resolution imaging spectroradiometer spectral reflectance, *J. Geophys. Res.*, 112, D13211, doi:10.1029/2006JD007811.
- Lin, S. (2004), A “vertically Lagrangian” finite-volume dynamical core for global models, *Mon. Weather Rev.*, 132(10), 2293–2307.
- Liou, K., and S. Ou (1989), The role of cloud microphysical processes in climate: An assessment from a one-dimensional perspective, *J. Geophys. Res.*, 94(D6), 8599–8607.
- Liu, H., D. Jacob, I. Bey, and R. Yantosca (2001), Constraints from Pb-210 and Be-7 on wet deposition and transport in a global three-dimensional chemical tracer model driven by assimilated meteorological fields, *J. Geophys. Res.*, 106(D11), 12,109–12,128.
- Malm, W., J. Sisler, D. Huffman, R. Eldred, and T. Cahill (1994), Spatial and seasonal trends in particle concentration and optical extinction in the United States, *J. Geophys. Res.*, 99(D1), 1347–1370.
- Maria, S., L. Russell, M. Gilles, and S. Myneni (2004), Organic aerosol growth mechanisms and their climate-forcing implications, *Science*, 306(5703), 1921–1924.

- Marticorena, B., and G. Bergametti (1995), Modeling the Atmospheric Dust Cycle: 1. Design of a soil-derived dust emission scheme, *J. Geophys. Res.*, 100(D8), 16,415–16,430.
- Martonchik, J., D. Diner, R. Kahn, B. Gaitley, and B. Holben (2004), Comparison of MISR and AERONET aerosol optical depths over desert sites, *Geophys. Res. Lett.*, 31(16), L16102, doi:10.1029/2004GL019807.
- Matichuk, R., P. Colarco, J. Smith, and O. Toon (2007), Modeling the transport and optical properties of smoke aerosols from African savanna fires during the Southern African Regional Science Initiative campaign (SAFARI 2000), *J. Geophys. Res.*, 112, D08203, doi:10.1029/2006JD007528.
- Matichuk, R., P. Colarco, J. Smith, and O. Toon (2008), Modeling the transport and optical properties of smoke plumes from South American biomass burning, *J. Geophys. Res.*, 113, D07208, doi:10.1029/2007JD009005.
- McCormick, R., and J. Ludwig (1967), Climate modification by atmospheric aerosols, *Science*, 156(3780), 1358–1359.
- Mitchell, J., Jr. (1971), The effect of atmospheric aerosols on climate with special reference to temperature near the earth's surface, *J. Appl. Meteorol.*, 10(4), 703–714.
- Monahan, E. C., D. E. Spiel, and K. L. Davidson (1986), A model of marine aerosol generation via whitecaps and wave disruption, in *Oceanic Whitecaps*, edited by E. C. Monahan and G. Mac Niocaill, pp. 167–174, D. Reidel, Dordrecht, The Netherlands.
- Morcrette, J.-J., et al. (2009), Aerosol analysis and forecast in the European centre for medium-range weather forecasts integrated forecast system: Forward modeling, *J. Geophys. Res.*, 114, D06206, doi:10.1029/2008JD011235.
- Nowottnick, E., P. Colarco, R. Ferrare, G. Chen, S. Ismail, B. Anderson, and E. Browell (2009), Online simulations of mineral dust aerosol distributions: Comparisons to NAMM observations and sensitivity to dust emission parameterization, *J. Geophys. Res.*, 115, D03202, doi:10.1029/2009JD012692.
- Park, R., D. Jacob, M. Chin, and R. Martin (2003), Sources of carbonaceous aerosols over the United States and implications for natural visibility, *J. Geophys. Res.*, 108(D12), 4355, doi:10.1029/2002JD003190.
- Lawson, S., et al. (2008), Goddard earth observing system chemistry-climate model simulations of stratospheric ozone-temperature coupling between 1950 and 2005, *J. Geophys. Res.*, 113(D12), D12103, doi:10.1029/2007JD009511.
- Perlitz, J., I. Tegen, and R. Miller (2001), Interactive soil dust aerosol model in the GISS GCM 1. Sensitivity of the soil dust cycle to radiative properties of soil dust aerosols, *J. Geophys. Res.*, 106(D16), 18,167–18,192.
- Prospero, J. (1999), Long-term measurements of the transport of African mineral dust to the southeastern United States: Implications for regional air quality, *J. Geophys. Res.*, 104(D13), 15,917–15,927.
- Ramanathan, V., P. Crutzen, J. Kiehl, and D. Rosenfeld (2001a), Atmosphere – Aerosols, climate, and the hydrological cycle, *Science*, 294(5549), 2119–2124.
- Ramanathan, V., et al. (2001b), Indian ocean experiment: An integrated analysis of the climate forcing and effects of the great Indo-Asian haze, *J. Geophys. Res.*, 106(D22), 28,371–28,398.
- Rasch, P., W. Collins, and B. Eaton (2001), Understanding the Indian Ocean Experiment (INDOEX) aerosol distributions with an aerosol assimilation, *J. Geophys. Res.*, 106(D7), 7337–7355.
- Reid, J., et al. (2003), Analysis of measurements of Saharan dust by airborne and ground-based remote sensing methods during the Puerto Rico Dust Experiment (PRIDE), *J. Geophys. Res.*, 108(D19), 8586, doi:10.1029/2002JD002493.
- Remer, L., et al. (2005), The MODIS aerosol algorithm, products, and validation, *J. Atmos. Sci.*, 62(4), 947–973.
- Remer, L., et al. (2008), Global aerosol climatology from the MODIS satellite sensors, *J. Geophys. Res.*, 113, D14S07, doi:10.1029/2007JD009661.
- Schluz, M., et al. (2006), Radiative forcing by aerosols as derived from the AeroCom present-day and pre-industrial simulations, *Atmos. Chem. Phys.*, 6, 5225–5246.
- Siebert, L., and T. Simkin (2002), Volcanoes of the World: An Illustrated Catalog of Holocene Volcanoes and their Eruptions, Smithsonian Institution, Global Volcanism Program Digital Information Series, GVP-3 (<http://www.volcano.si.edu/world/>)
- Singh, H., W. Brune, J. Crawford, D. Jacob, and P. Russell (2006), Overview of the summer 2004 intercontinental chemical transport experiment – North America (INTEX-A), *J. Geophys. Res.*, 111, D24S01, doi:10.1029/2006JD007905.
- Sinyuk, A., O. Torres, and O. Dubovik (2003), Combined use of satellite and surface observations to infer the imaginary part of refractive index of Saharan dust, *Geophys. Res. Lett.*, 30(2), 1081, doi:10.1029/2002GL016189.
- Smirnov, A., B. Holben, T. Eck, O. Dubovik, and I. Slutsker (2000), Cloud-screening and quality control algorithms for the AERONET database, *Remote Sens. Environ.*, 73(3), 337–349.
- Stephens, G., et al. (2002), The cloudsat mission and the a-train: A new dimension of space-based observations of clouds and precipitation, *Bull. Am. Meteorol. Soc.*, 83(12), 1771–1790.
- Streets, D., et al. (2009), Anthropogenic and natural contributions to regional trends in aerosol optical depth, 1980–2006, *J. Geophys. Res.*, 114, D00D18, doi:10.1029/2008JD011624.
- Swap, R., et al. (2003), Africa burning: A thematic analysis of the Southern African Regional Science Initiative (SAFARI 2000), *J. Geophys. Res.*, 108(D13), 8465, doi:10.1029/2003JD003747.
- Tanré, D., M. Herman, and Y. Kaufman (1996), Information on aerosol size distribution contained in solar reflected spectral radiances, *J. Geophys. Res.*, 101(D14), 19,043–19,060.
- Tanré, D., Y. Kaufman, M. Herman, and S. Mattoo (1997), Remote sensing of aerosol properties over oceans using the MODIS/EOS spectral radiances, *J. Geophys. Res.*, 102(D14), 16,971–16,988.
- Taylor, K. (2001), Summarizing multiple aspects of model performance in a single diagram, *J. Geophys. Res.*, 106(D7), 7183–7192.
- Tegen, I., and A. Lacis (1996), Modeling of particle size distribution and its influence on the radiative properties of mineral dust aerosol, *J. Geophys. Res.*, 101(D14), 19,237–19,244.
- Textor, C., et al. (2006), Analysis and quantification of the diversities of aerosol life cycles within AeroCom, *Atmos. Chem. Phys.*, 6, 1777–1813.
- Twomey, S. (1974), Pollution and the planetary albedo, *Atmos. Environ.*, 8(12), 1251–1256.
- van der Werf, G., J. Randerson, L. Giglio, G. Collatz, P. Kasibhatla, and A. Arellano (2006), Interannual variability in global biomass burning emissions from 1997 to 2004, *Atmos. Chem. Phys.*, 6, 3423–3441.
- Welton, E. J., J. R. Campbell, J. D. Spinhirne, and V. S. Scott (2001), Global monitoring of clouds and aerosols using a network of micro-pulse lidar systems, in *Lidar Remote Sensing for Industry and Environmental Monitoring*, edited by U. N. Singh, T. Itabe, and N. Sugimoto, Proc. SPIE, 4153, 151–158, for a conference in Sendai, Japan, 9–12, October 2000.
- Winker, D. M., J. Pelon, and M. P. McCormick (2003), The CALIPSO mission: Spaceborne lidar for observation of aerosols and clouds, Proc. SPIE Int. Soc. Opt. Eng., 4893, 1–11.
- Wiscombe, W. (1980), Improved Mie scattering algorithms, *Appl. Opt.*, 19(9), 1505–1509.
- Zhang, J., J. Reid, D. Westphal, N. Baker, and E. Hyer (2008), A system for operational aerosol optical depth data assimilation over global oceans, *J. Geophys. Res.*, 113, D10208, doi:10.1029/2007JD009065.

M. Chin, P. Colarco, and T. Diehl, Atmospheric Chemistry and Dynamics Branch, Laboratory for Atmospheres, NASA Goddard Space Flight Center, Greenbelt, MD 20771 USA.

A. da Silva, Global Modeling and Assimilation Office, Laboratory for Atmospheres, NASA Goddard Space Flight Center, Greenbelt, MD 20771, USA.